



## **Ionize Hard: Interstellar PO<sup>+</sup> Detection**

Downloaded from: <https://research.chalmers.se>, 2025-12-05 00:13 UTC

Citation for the original published paper (version of record):

Rivilla, V., García De La Concepción, J., Jimenez-Serra, I. et al (2022). Ionize Hard: Interstellar PO<sup>+</sup> Detection. *Frontiers in Astronomy and Space Sciences*, 9.  
<http://dx.doi.org/10.3389/fspas.2022.829288>

N.B. When citing this work, cite the original published paper.



# Ionize Hard: Interstellar PO<sup>+</sup> Detection

Víctor M. Rivilla<sup>1\*</sup>, Juan García De La Concepción<sup>1</sup>, Izaskun Jiménez-Serra<sup>1</sup>, Jesús Martín-Pintado<sup>1</sup>, Laura Colzi<sup>1</sup>, Belén Tercero<sup>2</sup>, Andrés Megías<sup>1</sup>, Álvaro López-Gallifa<sup>1</sup>, Antonio Martínez-Henares<sup>1</sup>, Sara Massalkhi<sup>1</sup>, Sergio Martín<sup>3,4</sup>, Shaoshan Zeng<sup>5</sup>, Pablo De Vicente<sup>2</sup>, Fernando Rico-Villas<sup>1</sup>, Miguel A. Requena-Torres<sup>6,7</sup> and Giuliana Cosentino<sup>8</sup>

<sup>1</sup>Centro de Astrobiología (CSIC-INTA), Madrid, Spain, <sup>2</sup>Observatorio Astronómico Nacional (OAN-IGN), Madrid, Spain, <sup>3</sup>European Southern Observatory, ALMA Department of Science, Santiago, Chile, <sup>4</sup>Joint ALMA Observatory, Department of Science Operations, Santiago, Chile, <sup>5</sup>Star and Planet Formation Laboratory, Cluster for Pioneering Research, RIKEN, Saitama, Japan, <sup>6</sup>Department of Astronomy, University of Maryland, College Park, MD, United States, <sup>7</sup>Department of Physics, Astronomy and Geosciences, Towson University, Towson, MD, United States, <sup>8</sup>Space, Earth and Environment Department, Chalmers University of Technology, Gothenburg, Sweden

## OPEN ACCESS

### Edited by:

Miriam Rengel,  
Max Planck Institute for Solar System  
Research, Germany

### Reviewed by:

Francois Lique,  
University of Rennes 1, France  
Marie-Aline Martin-Drumel,  
Centre National de la Recherche  
Scientifique (CNRS), France

### \*Correspondence:

Victor M. Rivilla  
vrivilla@cab.inta-csic.es

### Specialty section:

This article was submitted to  
Astrochemistry,  
a section of the journal  
Frontiers in Astronomy and Space  
Sciences

Received: 05 December 2021

Accepted: 28 February 2022

Published: 26 April 2022

### Citation:

Rivilla VM, García De La Concepción J, Jiménez-Serra I, Martín-Pintado J, Colzi L, Tercero B, Megías A, López-Gallifa Á, Martínez-Henares A, Massalkhi S, Martín S, Zeng S, De Vicente P, Rico-Villas F, Requena-Torres MA and Cosentino G (2022) Ionize Hard: Interstellar PO<sup>+</sup> Detection. *Front. Astron. Space Sci.* 9:829288. doi: 10.3389/fspas.2022.829288

We report the first detection of the phosphorus monoxide ion (PO<sup>+</sup>) in the interstellar medium. Our unbiased and very sensitive spectral survey toward the G+0.693–0.027 molecular cloud covers four different rotational transitions of this molecule, two of which ( $J = 1-0$  and  $J = 2-1$ ) appear free of contamination from other species. The fit performed, assuming local thermodynamic equilibrium conditions, yields a column density of  $N = (6.0 \pm 0.7) \times 10^{11} \text{ cm}^{-2}$ . The resulting molecular abundance with respect to molecular hydrogen is  $4.5 \times 10^{-12}$ . The column density of PO<sup>+</sup> normalized by the cosmic abundance of P is larger than those of NO<sup>+</sup> and SO<sup>+</sup>, normalized by N and S, by factors of 3.6 and 2.3, respectively. The  $N(\text{PO}^+)/N(\text{PO})$  ratio is  $0.12 \pm 0.03$ , more than one order of magnitude higher than that of  $N(\text{SO}^+)/N(\text{SO})$  and  $N(\text{NO}^+)/N(\text{NO})$ . These results indicate that P is more efficiently ionized than N and S in the ISM. We have performed new chemical models that confirm that the PO<sup>+</sup> abundance is strongly enhanced in shocked regions with high values of cosmic-ray ionization rates ( $10^{-15} - 10^{-14} \text{ s}^{-1}$ ), as occurring in the G+0.693–0.027 molecular cloud. The shocks sputter the interstellar icy grain mantles, releasing into the gas phase most of their P content, mainly in the form of PH<sub>3</sub>, which is converted into atomic P, and then ionized efficiently by cosmic rays, forming P<sup>+</sup>. Further reactions with O<sub>2</sub> and OH produces PO<sup>+</sup>. The cosmic-ray ionization of PO might also contribute significantly, which would explain the high  $N(\text{PO}^+)/N(\text{PO})$  ratio observed. The relatively high gas-phase abundance of PO<sup>+</sup> with respect to other P-bearing species stresses the relevance of this species in the interstellar chemistry of P.

**Keywords:** phosphorus, interstellar: abundances, interstellar: clouds, astrochemistry, interstellar: ions

## 1 INTRODUCTION

Phosphorus (P), along with carbon (C), hydrogen (H), oxygen (O), nitrogen (N), and sulfur (S), is one of the key elements for the development of life (CHONPS). This is because P-bearing compounds, and in particular phosphates (PO<sub>4</sub><sup>3-</sup>), are unique in forming large biomolecules, such as deoxyribonucleic acid (DNA) and ribonucleic acid (RNA), phospholipids (the structural components of cellular membranes), and the adenosine triphosphate (ATP)

molecule, which stores the chemical energy within cells. However, while the P abundance in living organisms is relatively high, for e.g. P/H  $\sim 10^{-3}$  in bacteria (Fagerbakke et al., 1996), the abundance of P in the universe is several orders of magnitude lower, for e.g. P/H  $\sim 3 \times 10^{-7}$  in the solar photosphere (Asplund et al., 2009), much lower than that of other biogenic elements. Due to this low cosmic availability of P, the detection of P-bearing molecules beyond our planet is challenging.

In our solar system, phosphine (PH<sub>3</sub>) has been observed in the atmospheres of Jupiter and Saturn (Bregman et al., 1975; Ridgway et al., 1976). P has been identified in meteorites in the form of the mineral schreibersite (Pasek and Lauretta 2005) and phosphoric acids (Schwartz 2006). Recently, the measurements of the Rosetta spacecraft detected P in the comet 67P/Churyumov–Gerasimenko (Altwegg et al., 2016), which is predominantly in the form of phosphorus monoxide, PO (Rivilla et al., 2020a). In the circumstellar envelopes of evolved stars, six different simple P-bearing molecules, up to four atoms, have been detected: PN, PO, CP, HCP, C<sub>2</sub>P, and PH<sub>3</sub> (e.g. Guelin et al., 1990; Agúndez et al., 2007; Tenenbaum et al., 2007; Halfen et al., 2008; Agúndez et al., 2014). However, in diffuse and molecular clouds and star-forming regions, only P<sup>+</sup>, PN, and PO have been detected. The ion P<sup>+</sup> was discovered in several diffuse clouds (Jura and York 1978), although no P-bearing molecules have been identified toward these regions despite deep observational searches (Chantzos et al., 2020). In molecular clouds and star-forming regions, only PN and PO have been identified in different environments (Turner and Bally 1987; Ziurys 1987; Fontani et al., 2016, 2019; Lefloch et al., 2016; Rivilla et al., 2016; Rivilla et al., 2018, 2020a; Bergner et al., 2019; Bernal et al., 2021). Recently, PN has been detected toward molecular cloud complexes within the central region of the starburst galaxy NCG 253 (Haasler et al., 2022).

In recent years, several efforts have been made to better understand the chemistry of P in the ISM, based on the comparison of the molecular abundances derived from observations and the predictions from dedicated chemical models (e.g. Thorne et al., 1984; Fontani et al., 2016; Rivilla et al., 2016; Jiménez-Serra et al., 2018; Chantzos et al., 2020) and quantum chemical calculations (Mancini et al., 2020; García de la Concepción et al., 2021). However, the small number of P-bearing species so far detected prevents us from establishing strong constraints on the chemical networks, in which many possible chemical pathways are still unexplored and poorly characterized. For this reason, it is needed to further expand the census of P-bearing species in the ISM, and their molecular abundances.

One of the most promising candidates is the phosphorus monoxide ion, PO<sup>+</sup>. This molecule presents a large dipole moment of  $\sim 3.44$  Debye (from calculations of Peterson and Woods 1990), which might allow its detection through rotational spectroscopy even with relatively low abundance. Moreover, other monoxide ions of biogenic elements such as

SO<sup>+</sup>, CO<sup>+</sup>, and NO<sup>+</sup> have already been detected previously in the ISM (Turner 1992; Latter et al., 1993; Cernicharo et al., 2014, respectively). Previous detections of the monoxide ion SO<sup>+</sup> have shown that this species is strongly enhanced in shocked gas, following the release of S and S-bearing molecules from the grain mantles and by subsequent ionization, being the main formation route, through the reaction S<sup>+</sup> + OH  $\rightarrow$  SO<sup>+</sup> + H (Herbst and Leung 1989; Neufeld and Dalgarno 1989; Turner 1992, 1996; Podio et al., 2014).

Similar to S, P is considered to be (even more) depleted in interstellar dust grains (Lefloch et al., 2016; Rivilla et al., 2016), and shocks have been invoked as a key agent for the formation of P-bearing species by gas-phase chemistry (Lefloch et al., 2016; Jiménez-Serra et al., 2018; Mininni et al., 2018; Rivilla et al., 2020a). Therefore, the best targets to search for PO<sup>+</sup> are regions with the presence of shocks and sources of ionization, such as high cosmic-ray ionization rates, and with previous detections of P-bearing species.

The molecular cloud G+0.693–0.027 (hereafter G+0.693), located in the Sgr B2 complex in the Central Molecular Zone (CMZ) of our galaxy, fulfills all of these conditions. Its chemistry is strongly affected by large-scale shocks (e.g. Martín et al., 2008; Requena-Torres et al., 2008; Zeng et al., 2020), likely produced by a cloud–cloud collision (Zeng et al., 2020). Moreover, it is well known that the cosmic-ray ionization rate in the CMZ can be above  $\zeta \sim 10^{-15} \text{ s}^{-1}$  (Goto et al., 2014), which is more than two orders of magnitude higher than the standard local Galactic value (Padovani et al., 2009). All these and the detection of PO and PN (Rivilla et al., 2018) toward G+0.693 make this cloud one of the best targets to search for new P-bearing species, and in particular PO<sup>+</sup>.

In this work, we report the first detection of PO<sup>+</sup> in the ISM toward G+0.693. The molecular ions SO<sup>+</sup> and NO<sup>+</sup> have also been detected, and the latter detected for the second time in the ISM. We have also analyzed their neutral counterparts PO, SO, and NO and computed the relative ratio among neutrals and ions. Finally, we have discussed about their possible chemistry in the ISM, including new chemical modeling of PO<sup>+</sup>.

## 2 OBSERVATIONS

We have used an unbiased and sensitive spectral line survey toward G+0.693 carried out with three telescopes: Yebes 40m telescope (Guadalajara, Spain), IRAM 30m telescope (Pico Veleta, Spain), and APEX telescope (Atacama, Chile). The observations were centered at  $\alpha(\text{J2000.0}) = 17^{\text{h}}47^{\text{m}}22^{\text{s}}$  and  $\delta(\text{J2000.0}) = -28^{\circ}21'27''$ . The position switching mode was used in all the observations with the off position located at  $\Delta\alpha = -885''$  and  $\Delta\delta = 290''$  from the source position. The line intensity of the spectra was measured in units of  $T_{\text{A}}^*$  as the molecular emission toward G+0.693 is extended over the beam (Requena-Torres et al., 2006, 2008; Zeng et al., 2018).

## 2.1 IRAM 30m Observations

We used the dual polarization receiver EMIR connected to the fast Fourier transform spectrometers (FFTSs), which provided a channel width of 200 kHz in the following spectral windows: 71.76–116.72 GHz, 124.77–175.5 GHz, and 223.307–238.29 GHz. Detailed information of the observational survey is presented in Rivilla et al. (2021a) and Rivilla et al. (2021b). The half power beam width (HPBW) of the telescope ranges from  $\sim 10.3''$  to  $\sim 34.3''$  in the spectral range covered.

## 2.2 Yebes 40m Observations

We have performed new observations using the Yebes 40m telescope. A total of 29 observing sessions between March and June 2021 (total observing time  $\sim 100$  h) were performed, as part of the project 21A014 (PI: Rivilla). The NANOCOSMOS Q-band (7mm) HEMT receiver was used, which enables ultra-broadband observations ( $\sim 18$  GHz) in two linear polarizations (Tercero et al., 2021). The receiver was connected to 16 FFTSs providing a channel width of 38 kHz and a bandwidth of 18.5 GHz per polarization. We observed two different spectral setups centered at 41.400 and 42.300 GHz. The total frequency range is 31.07–50.42 GHz. We performed an initial data inspection and reduction using the CLASS module of the GILDAS package<sup>1</sup> and our own Python-based scripts<sup>2</sup>. The comparison of the spectra of the two spectral setups was used to identify possible spurious lines in the IF. Telescope pointing and focus were checked every 1 or 2 h through pseudo-continuum observations toward the red hypergiant star VX Sgr. The final spectra were smoothed to  $2 \text{ km s}^{-1}$ . The half power beam width (HPBW) of the telescope was  $\sim 39''$  at 44 GHz.

## 2.3 APEX Observations

We have also used data from two projects observed in the service mode using the APEX telescope: O-0108.F-9308A-2021 (PI: Rivilla) and E-0108.C-0306A-2021 (PI: Rivilla). We used the NFLASH230 receiver connected to two FFTS backends, which provide a simultaneous coverage of two sidebands of 7.9 GHz each separated by 8 GHz. The spectral resolution was 250 kHz. The project O-0108.F-9308A-2021 was observed during 10 different observing runs from July 11 to September 26, 2021, with a total observing time of 23.4 h. We used two different frequency setups slightly shifted in frequency (262.0 and 262.3 GHz) to check for possible spurious lines from the image band. The total spectral range covered was 243.94–252.13 GHz and 260.17–268.38 GHz. The precipitable water vapor (pwv) during the observations was in the range of 0.7–3.6 mm. The project E-0108.C-0306A-2021 was observed during two different observing runs:

October 31 and November 1, 2021. The total observing time was 5.8 h. We used two different frequency setups slightly shifted in frequency (224.0 and 224.1 GHz) to check for possible spurious lines from the image band. The total spectral range covered was 217.93–225.93 GHz and 234.18–242.18 GHz. The precipitable water vapor (pwv) during the observations was in the range of 0.9–2.2 mm. The final spectra from both projects were smoothed to 1 MHz, which translates into a velocity resolution of  $1.1\text{--}1.4 \text{ km s}^{-1}$  in the frequency ranges observed. The half power beam width (HPBW) of these APEX observations is  $\sim 23'' - 28''$  in the frequency range observed.

## 3 ANALYSIS AND RESULTS

The identification and fitting of the molecular lines were performed using the SLIM (Spectral Line Identification and Modeling) tool within the MADCUBA package<sup>3</sup> (version 09/11/2021; Martín et al., 2019). SLIM uses the molecular databases of the Cologne Database for molecular spectroscopy (CDMS, Endres et al., 2016) and the Jet Propulsion Laboratory (JPL; Pickett et al., 1998) to generate synthetic spectra under the assumption of local thermodynamic equilibrium (LTE). In **Appendix A**, we list the details of the molecular spectroscopy of all the molecules analyzed in this work. To evaluate if the transitions are blended with emission from other species, we have also considered the LTE model that predicts the total contribution of more than 120 species than have been identified so far toward G+0.693 (e.g., Requena-Torres et al., 2008; Zeng et al., 2018; Rivilla et al., 2019, 2020b; Jiménez-Serra et al., 2020; Rivilla et al., 2021a; Rivilla et al., 2021b; Zeng et al., 2021; Rodríguez-Almeida et al., 2021a,b). To derive the physical parameters of the molecular emission, we used the AUTOFIT tool of SLIM, which finds the best fit between the observed spectra and the predicted LTE model (see details in Martín et al., 2019). The free parameters of the LTE model were as follows: molecular column density ( $N$ ), excitation temperature ( $T_{\text{ex}}$ ), linewidth (or full width at half maximum,  $FWHM$ ), and velocity ( $v_{\text{LSR}}$ ).

### 3.1 PO<sup>+</sup> Detection

We have used the molecular spectroscopy from the laboratory work by Petrmichl et al. (1991). The  $J = 1-0$  and  $J = 2-1$  transitions of PO<sup>+</sup> at 47.024 GHz and 94.047 GHz (**Table 1**), respectively, have been detected in our survey, as shown in the upper panels of **Figure 1**. This is the first detection of PO<sup>+</sup> reported in the ISM. We note that the laboratory work by Petrmichl et al. (1991) measured PO<sup>+</sup> transitions in the range 140–470 GHz, and thus the two unblended transitions detected in the present work are actually the very first observation of these

<sup>1</sup><https://www.iram.fr/IRAMFR/GILDAS>.

<sup>2</sup><https://www.python.org>.

<sup>3</sup>Madrid Data Cube Analysis on ImageJ is software developed at the Center of Astrobiology (CAB) in Madrid; <http://cab.inta-csic.es/madcuba/>.

two lines. The  $J = 3-2$  and  $J = 4-3$  transitions were also covered by the survey. The former transition, at 141.070 GHz, is heavily blended with bright emission from H<sup>13</sup>CCCN(16–15) (see the right panel of **Figure 2**). The  $J = 4-3$  transition at 235.107 GHz (not shown here) is also strongly blended with an unidentified species. We note that the expected line intensity of this higher-energy PO<sup>+</sup> transition (**Table 1**), according to the best LTE fit (see the following), is  $<0.25$  mK, which is lower than the noise level of the observed spectra.

The upper panels of **Figure 1** show that the spectral profiles of the  $J = 1-0$  and  $J = 2-1$  transitions are not completely identical, with the 1–0 transition showing a more prominent wing at blue-shifted velocities. This is consistent with the observed profiles of other P-bearing molecule such as PN. The lower panels of **Figure 1** show that the lower the energy level of the PN transition, the more prominent the wing at blue-shifted velocities is, as also observed in PO<sup>+</sup>. This suggests that there are two different velocity components, one peaking at  $\sim 70$  km s<sup>-1</sup> and another one at more blue-shifted velocities (producing the wing of the 1–0 transitions), under different excitation conditions. These two velocity components have also been identified in several other molecular species (Colzi et al., 2022).

For simplicity, to perform the fit of PO<sup>+</sup>, we have considered only the  $\sim 70$  km s<sup>-1</sup> velocity component, which dominates the emission of the two transitions. To run AUTOFIT, we have considered the  $J = 1-0$ ,  $J = 2-1$ , and  $J = 3-2$  transitions, taking also the contribution of all the other species into account. We have fixed the velocity to  $v_{\text{LSR}} = 70$  km s<sup>-1</sup>, the linewidth to  $FWHM = 18$  km s<sup>-1</sup>, and the  $T_{\text{ex}}$  to 4.5 K, which is the value derived when fitting the transitions of PN shown in the lower panels of **Figure 1** (Rivilla et al., in preparation). The result of the fit of PO<sup>+</sup> is shown in **Figure 2**. We note that the JPL entry used to perform the fit considers a dipole moment of  $\mu = 3.44$  Debye, calculated by Peterson and Woods (1990). In **Appendix B**, we present higher level calculations of the PO<sup>+</sup> dipole moment, which gives a value of  $\mu = 3.13$  Debye. Therefore, to calculate the final molecular column density, we have multiplied the value derived using the JPL entry by a factor of  $(3.44/3.13046)^2 = 1.21$ . The derived value of the PO<sup>+</sup> column density is  $(6.0 \pm 0.7) \times 10^{11}$  cm<sup>-2</sup> (**Table 2**). This translates into a molecular abundance with respect to molecular hydrogen of  $(4.5 \pm 1.1) \times 10^{-12}$ , using the value of  $N(\text{H}_2) = 1.35 \times 10^{23}$  cm<sup>-2</sup> from Martín et al. (2008).

### 3.2 PO

To study the relative abundance of PO<sup>+</sup> with respect to its neutral counterpart, we have also analyzed the molecular emission of PO. This molecule was already detected toward G+0.693 by Rivilla et al. (2018) using a previous less sensitive spectral survey carried out using the IRAM 30m (Zeng et al., 2018). We repeat here the analysis using the data from the new deeper survey. The  $J = 5/2-3/2$ ,  $\Omega = 1/2$  quadruplet of PO (with  $E_{\text{up}} = 8.4$  K, **Table 1**) is displayed in **Figure 3**. The  $F = 3-2$   $l = e$  transition is completely unblended (see also the middle panel of **Figure 1**), while the  $F = 3-2$   $l = f$  is slightly blended with a very weak line of ethanolamine

(NH<sub>2</sub>CH<sub>2</sub>CH<sub>2</sub>OH, Rivilla et al., 2021a), and an unidentified species. The other two transitions appear blended with other species already identified in G+0.693, which are indicated in the last column of **Table 1**. The  $J = 7/2-5/2$ ,  $\Omega = 1/2$  quadruplet of PO at 152 GHz (with  $E_{\text{up}} = 15.7$  K), which is also covered by our survey, is expected too weak to be detected, with predicted line intensities of  $\leq 4$  mK, according to the LTE fit of the  $J = 5/2-3/2$ ,  $\Omega = 1/2$  transitions (see the following), which is lower than the noise of the data at that frequency ( $\sim 5$  mK).

To perform the fit, we have used the  $J = 5/2-3/2$ ,  $\Omega = 1/2$   $F = 3-2$   $l = e$  unblended transition. We fixed  $T_{\text{ex}}$  to 4.5 K, as for PO<sup>+</sup>, leaving  $N$ ,  $FWHM$ , and  $v_{\text{LSR}}$  as free parameters. The results are shown in **Table 2**. We obtained  $v_{\text{LSR}} = 69.5 \pm 1.4$  and  $FWHM = 15 \pm 3$  km s<sup>-1</sup>, which are consistent to the fixed values used for PO<sup>+</sup>. The derived column density is  $(0.5 \pm 0.1) \times 10^{13}$  cm<sup>-2</sup>, a factor of 1.6 lower than that reported by Rivilla et al. (2018) previously. Using this value, we obtained a molecular column density ratio PO<sup>+</sup>/PO =  $0.12 \pm 0.03$ .

### 3.3 SO<sup>+</sup>, S<sup>18</sup>O, and <sup>34</sup>SO

We show in **Figures 4–6** the molecular transitions of SO<sup>+</sup>, <sup>34</sup>SO, and S<sup>18</sup>O, respectively, detected toward G+0.693. We note that the JPL entry used for SO<sup>+</sup> (see **Table A1** in **Appendix A**) assumes a dipole moment of  $\mu = 1$ , while theoretical *ab initio* calculations reported in Turner (1992) from a private communication from Peterson and Woods derived  $\mu = 2.3 \pm 0.2$  Debye. As for PO<sup>+</sup>, in **Appendix B**, we have performed new higher level calculations for SO<sup>+</sup>, which result in a dipole moment of  $\mu = 2.016$ . Therefore, we have corrected the column density derived by AUTOFIT by the factor  $(1/2.016)^2$ . The derived physical parameters from the SO<sup>+</sup> emission are shown in **Table 2**. We obtained  $T_{\text{ex}} = 8.0 \pm 0.3$  K,  $v_{\text{LSR}} = 68.8 \pm 0.3$  km s<sup>-1</sup>,  $FWHM = 18.0 \pm 0.7$  km s<sup>-1</sup>, and  $N = (1.34 \pm 0.07) \times 10^{13}$  cm<sup>-2</sup>.

Since the SO transitions detected toward G+0.693 are optically thick, we have analyzed its optically thin isotopologues to better derive its column density. For S<sup>18</sup>O, only a single transition is detected (**Figure 6**), so we have fixed  $T_{\text{ex}}$  to the value derived for <sup>34</sup>SO, which is  $6.9 \pm 0.1$  K. The physical parameters derived by AUTOFIT are shown in **Table 2**. Using the derived column densities for both isotopologues and assuming the isotopic ratios <sup>32</sup>S/<sup>34</sup>S = 22 and <sup>16</sup>O/<sup>18</sup>O = 250 in the CMZ (Wilson and Rood 1994), we have derived that the column density of SO is  $(142 \pm 4) \times 10^{13}$  cm<sup>-2</sup> and  $(300.6 \pm 0.7) \times 10^{13}$  cm<sup>-2</sup>, from <sup>34</sup>SO and S<sup>18</sup>O, respectively. Since the most optically thin isotopologue is S<sup>18</sup>O, we use its value hereafter to compute relative molecular abundances ratios. The ratio SO<sup>+</sup>/SO =  $0.0045 \pm 0.0003$ , which is a factor of  $\sim 30$  lower than the PO<sup>+</sup>/PO ratio. Note that even using the lower limit of  $(142 \pm 4) \times 10^{13}$  cm<sup>-2</sup>, the ratio SO<sup>+</sup>/SO would still be a factor of 15 lower than that measured for the PO<sup>+</sup>/PO ratio.

### 3.4 NO<sup>+</sup> and NO

We show in **Figure 7** the detection of the  $N = 2-1$  transition of NO<sup>+</sup>, which is the only transition of this species that falls in the frequency range covered by our survey. This is the second detection of this species toward the ISM, after the one reported toward the cold dense core Barnard 1 – b by

**TABLE 1** | List of targeted transitions of PO<sup>+</sup>, SO<sup>+</sup>, and NO<sup>+</sup> ions and their associated neutrals PO, S<sup>18</sup>O, <sup>34</sup>SO, and NO.

Molecule	Frequency (GHz)	Transition	log A <sub>ul</sub> (s <sup>-1</sup> )	g <sub>u</sub>	E <sub>u</sub> (K)	Blending <sup>(a)</sup>
PO <sup>+</sup>	47.024252	$J = 1-0$	-5.32112	3	2.3	Unblended
PO <sup>+</sup>	94.047798	$J = 2-1$	-4.33884	5	6.8	Unblended
PO <sup>+</sup>	141.069934	$J = 3-2$	-3.78062	7	13.5	H <sup>13</sup> CCCN
PO <sup>+</sup>	235.107153	$J = 5-4$	-3.08956	11	33.9	Un
PO	108.99844500	$J = 5/2-3/2, \Omega = 1/2, F = 3-2, l = e$	-4.67120	7	8.4	Unblended
PO	109.04539600	$J = 5/2-3/2, \Omega = 1/2, F = 2-1, l = e$	-4.71676	5	8.4	s - C <sub>2</sub> H <sub>5</sub> CHO
PO	109.20620000	$J = 5/2-3/2, \Omega = 1/2, F = 3-2, l = f$	-4.66892	7	8.4	NH <sub>2</sub> CH <sub>2</sub> CH <sub>2</sub> OH + Un
PO	109.28118900	$J = 5/2-3/2, \Omega = 1/2, F = 2-1, l = f$	-4.71433	5	8.4	aGg - (CH <sub>2</sub> OH) <sub>2</sub>
SO <sup>+</sup>	115.804405	$J = 5/2-3/2, \Omega = 1/2, l = e$	-5.14768	6	8.9	Unblended
SO <sup>+</sup>	116.179947	$J = 5/2-3/2, \Omega = 1/2, l = f$	-5.14351	6	8.9	Unblended
SO <sup>+</sup>	162.198598	$J = 7/2-5/2, \Omega = 1/2, l = e$	-4.67885	8	16.7	Unblended
SO <sup>+</sup>	162.574058	$J = 7/2-5/2, \Omega = 1/2, l = f$	-4.67575	8	16.7	Unblended
SO <sup>+</sup>	208.590016	$J = 9/2-7/2, \Omega = 1/2, l = e$	-4.33524	10	26.7	Unblended
SO <sup>+</sup>	208.965420	$J = 9/2-7/2, \Omega = 1/2, l = f$	-4.33294	10	26.8	Unblended
S <sup>18</sup> O	93.267270	$N_J = 2_3-1_2$	-5.02955	7	8.7	Unblended
<sup>34</sup> SO	84.4106900	$N_J = 2_2-1_1$	-5.30558	5	19.2	Unblended
<sup>34</sup> SO	97.7153170	$N_J = 3_2-2_1$	-4.96948	7	9.1	Unblended
<sup>34</sup> SO	106.743244	$N_J = 2_1-3_2$	-4.99699	5	20.9	Unblended
<sup>34</sup> SO	126.613930	$N_J = 3_3-2_2$	-4.67350	7	25.3	Unblended
<sup>34</sup> SO	135.775728	$N_J = 4_3-3_2$	-4.52226	9	15.6	Unblended
<sup>34</sup> SO	175.352766	$N_J = 5_4-4_3$	-4.17742	11	24.0	Unblended
<sup>34</sup> SO	215.839920	$N_J = 6_5-5_4$	-3.89897	13	34.4	Unblended
NO <sup>+</sup>	238.3831574	$N = 2-1$	-5.0635	15	17.1	Unblended
NO	150.1764800	$J = 3/2-1/2, \Omega = 1/2^+, F = 5/2-3/2$	-6.4802	6	7.2	Unblended
NO	150.1987600	$J = 3/2-1/2, \Omega = 1/2^+, F = 3/2-1/2$	-6.7355	4	7.2	Un
NO	150.2187300	$J = 3/2-1/2, \Omega = 1/2^+, F = 3/2-3/2$	-6.8323	4	7.2	Autoblended
NO	150.2256600	$J = 3/2-1/2, \Omega = 1/2^+, F = 1/2-1/2$	-6.5313	2	7.2	Autoblended
NO	150.2456356	$J = 3/2-1/2, \Omega = 1/2^+, F = 1/2-3/2$	-7.4343	2	7.2	HOCO <sup>+</sup>
NO	150.3752987	$J = 3/2-1/2, \Omega = 1/2^-, F = 1/2-3/2$	-7.4319	2	7.2	Unblended
NO	150.4391200	$J = 3/2-1/2, \Omega = 1/2^-, F = 3/2-3/2$	-6.8297	4	7.2	c - C <sub>3</sub> H <sub>2</sub>
NO	150.5465200	$J = 3/2-1/2, \Omega = 1/2^-, F = 5/2-3/2$	-6.4771	6	7.2	Unblended
NO	150.5805600	$J = 3/2-1/2, \Omega = 1/2^-, F = 1/2-1/2$	-6.5282	2	7.2	Unblended
NO	150.6443400	$J = 3/2-1/2, \Omega = 1/2^-, F = 3/2-1/2$	-6.7321	4	7.2	Unblended
NO	250.4368480	$J = 5/2-3/2, \Omega = 1/2^+, F = 7/2-5/2$	-5.7349	8	19.2	Autoblended
NO	250.4406590	$J = 5/2-3/2, \Omega = 1/2^+, F = 5/2-3/2$	-5.8105	6	19.2	Autoblended
NO	250.4485300	$J = 5/2-3/2, \Omega = 1/2^+, F = 3/2-1/2$	-5.8597	4	19.2	Autoblended
NO	250.4754140	$J = 5/2-3/2, \Omega = 1/2^+, F = 3/2-3/2$	-6.3546	4	19.2	Autoblended + NS <sup>+</sup>
NO	250.4829390	$J = 5/2-3/2, \Omega = 1/2^+, F = 5/2-5/2$	-6.5307	6	19.2	Autoblended + NS <sup>+</sup>
NO	250.5177030	$J = 5/2-3/2, \Omega = 1/2^+, F = 3/2-5/2$	-7.7347	4	19.2	Un
NO	250.6458000	$J = 5/2-3/2, \Omega = 1/2^-, F = 3/2-5/2$	-7.7332	4	19.3	Un
NO	250.7082450	$J = 5/2-3/2, \Omega = 1/2^-, F = 5/2-5/2$	-6.5290	6	19.3	Unblended
NO	250.7531400	$J = 5/2-3/2, \Omega = 1/2^-, F = 3/2-3/2$	-6.3529	4	19.3	Unblended
NO	250.7964360	$J = 5/2-3/2, \Omega = 1/2^-, F = 7/2-5/2$	-5.7330	8	19.3	Autoblended
NO	250.8155940	$J = 5/2-3/2, \Omega = 1/2^-, F = 5/2-3/2$	-5.8087	6	19.3	Autoblended
NO	250.8169540	$J = 5/2-3/2, \Omega = 1/2^-, F = 3/2-1/2$	-5.8579	4	19.3	Autoblended

We provide the transition frequencies, quantum numbers, the base 10 logarithm of Einstein coefficients (log A<sub>ul</sub>), the upper state degeneracy (g<sub>u</sub>), and the upper energy level (E<sub>u</sub>). The last column states if the transitions are unblended or blended with another molecular species.

<sup>a</sup>We indicate if the transition is blended with an already identified species, with an unidentified species (Un), or autoblended (with a transition close in frequency of the same molecule).

Cernicharo et al. (2014), using the same transition. Since only a single transition is detected, we fixed the  $T_{\text{ex}}$  to the value derived from NO, which is 11.2 K (see the following). The result of the fit is shown in Table 2. We obtained a column density of  $(3.89 \pm 0.05) \times 10^{13} \text{ cm}^{-2}$ .

NO was already reported toward G+0.693 in Zeng et al. (2020), who detected the  $J = 3/2-1/2$  transitions (see Table 1) using a

previous IRAM 30m survey (Zeng et al., 2018). Using data from the new survey, we have also detected the higher energy  $J = 5/2-3/2$  transitions with APEX (Table 1), which allow us to constrain its excitation temperature more accurately. We have obtained  $T_{\text{ex}} = 11.2 \pm 0.2 \text{ K}$  and a column density of  $(1.58 \pm 0.03) \times 10^{16} \text{ cm}^{-2}$ , which is a factor of  $\sim 2$  lower than that reported by Zeng et al. (2020). The best LTE fit slightly underestimates ( $\sim 10\%$ ) the line intensities of

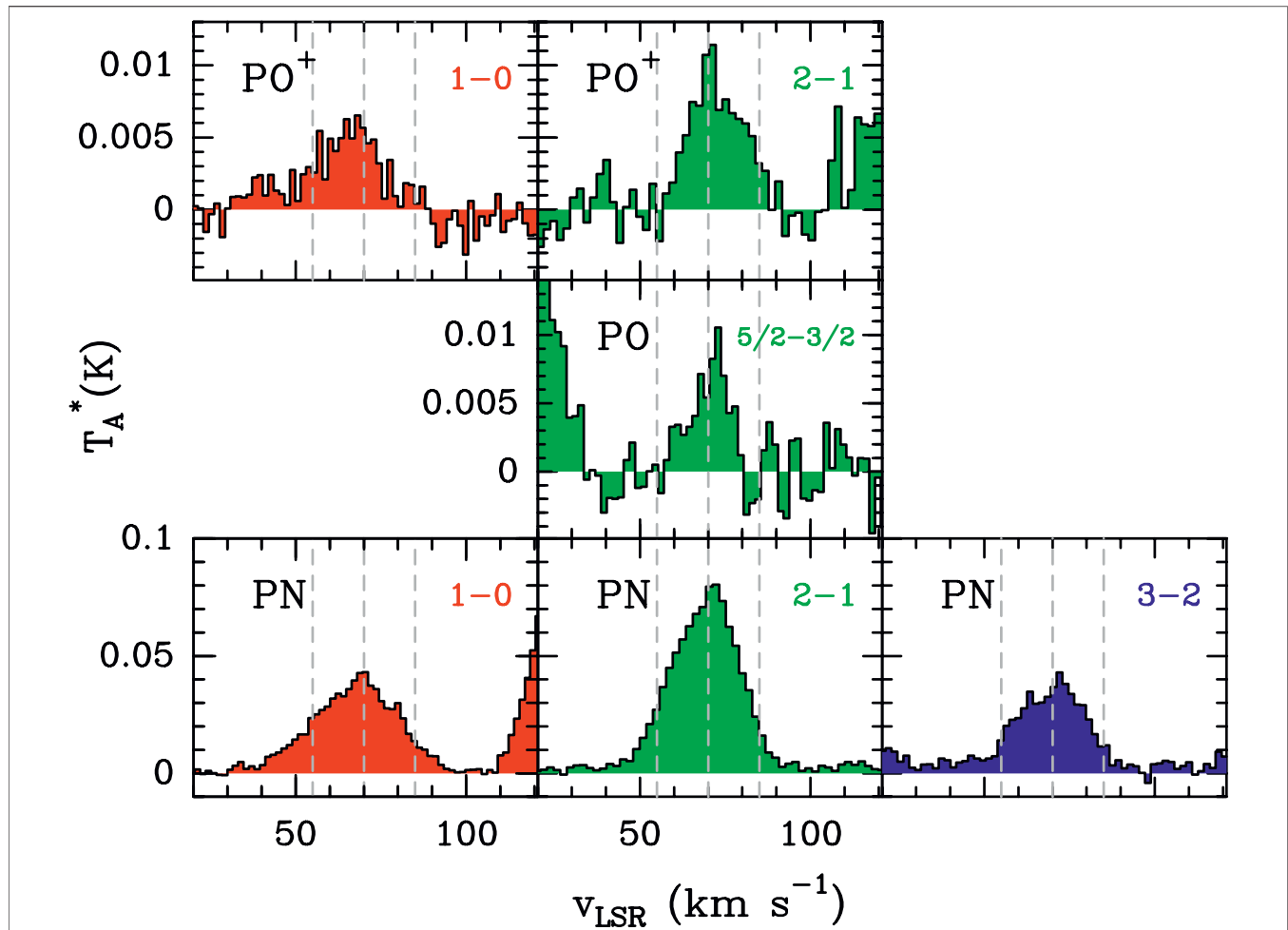


**FIGURE 1** | Spectral profiles of the molecular transitions of the P-bearing species detected toward G+0.693 (see **Table 1**):  $\text{PO}^+$  (upper panels), PO (middle panel), and PN (lower panels). The left/middle/right columns show transitions with  $E_{\text{up}} = 2.3/6.8 - 8.4/13.5$  K, indicated with red/green/blue histograms, respectively. The gray vertical dashed lines indicate the velocities  $70 \text{ km s}^{-1}$  and  $70 \pm 15 \text{ km s}^{-1}$ .

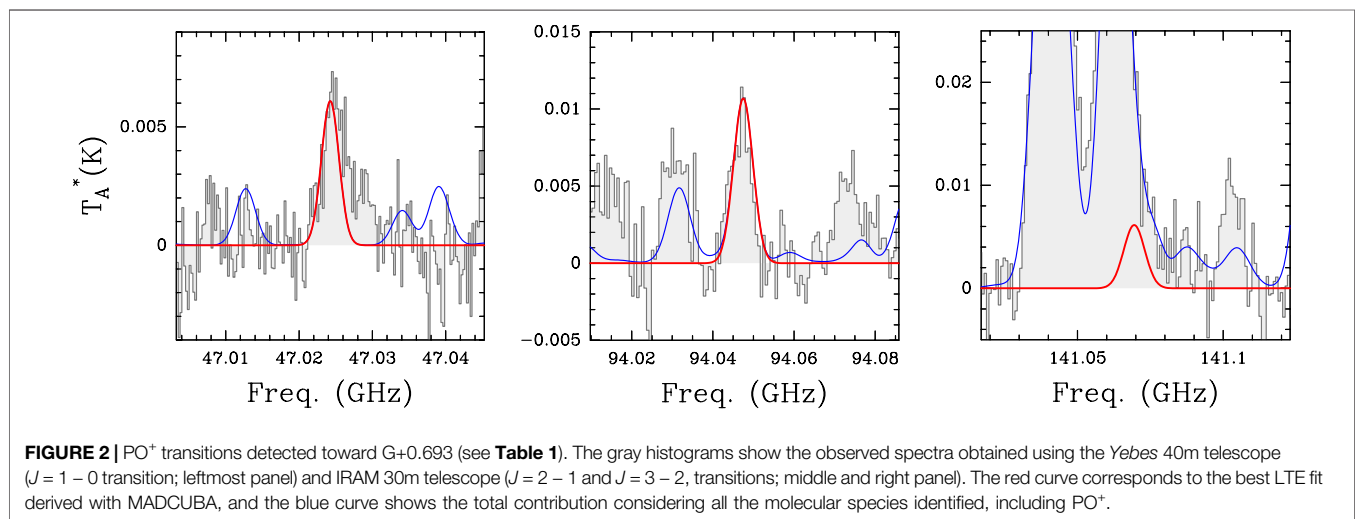


**FIGURE 2** |  $\text{PO}^+$  transitions detected toward G+0.693 (see **Table 1**). The gray histograms show the observed spectra obtained using the *Yebes* 40m telescope ( $J = 1 - 0$  transition; leftmost panel) and IRAM 30m telescope ( $J = 2 - 1$  and  $J = 3 - 2$ , transitions; middle and right panel). The red curve corresponds to the best LTE fit derived with MADCUBA, and the blue curve shows the total contribution considering all the molecular species identified, including  $\text{PO}^+$ .

**TABLE 2** | Derived physical parameters of the molecules toward G+0.693 analyzed in this work.

Molecule	$N$ ( $\times 10^{13}$ cm <sup>-2</sup> )	$T_{\text{ex}}$ (K)	$v_{\text{LSR}}$ (km s <sup>-1</sup> )	$\text{FWHM}$ (km s <sup>-1</sup> )	Abundance <sup>a</sup> ( $\times 10^{-10}$ )
PO <sup>+</sup>	0.060 ± 0.007	4.5	70	18	0.045
PO	0.49 ± 0.09	4.5	69.5 ± 1.4	15 ± 3	0.36
SO <sup>+</sup>	1.34 ± 0.07	8.0 ± 0.3	68.8 ± 0.3	18.0 ± 0.7	1.0
<sup>34</sup> SO	6.5 ± 0.2	6.9 ± 0.1	68.3 ± 0.2	22.1 ± 0.4	4.8
S <sup>18</sup> O	1.20 ± 0.03	6.9	67.9 ± 0.3	24.8 ± 0.7	0.89
NO <sup>+</sup>	3.89 ± 0.05	11.2	68.1 ± 0.2	18.1 ± 0.3	3.2
NO	1580 ± 30	11.2 ± 0.2	67.4 ± 0.1	20.4 ± 0.3	1170

<sup>a</sup>We adopted  $N_{\text{H}_2} = 1.35 \times 10^{23}$  cm<sup>-2</sup>, from Martín et al. (2008).

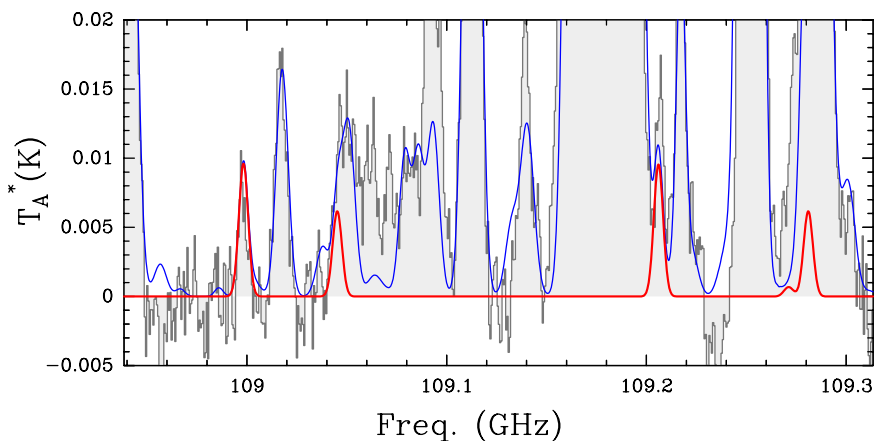


**FIGURE 3** | PO transitions detected toward G+0.693 (see **Table 1**). The gray histogram shows the observed spectra obtained using the IRAM 30m telescope. The red curve corresponds to the best LTE fit derived with MADCUBA, and the blue curve shows the total contribution considering all the molecular species identified, including PO.

the transitions at 150 GHz. This small discrepancy is within the typical uncertainties in the calibration of the IRAM 30m data, and therefore the LTE fit reproduces reasonably well both sets of lines, within the calibration uncertainties. The derived ratio NO<sup>+</sup>/NO is  $0.00245 \pm 0.00005$ , which is very similar to that derived in the cold core Barnard 1-b of  $\sim 0.002$  (Cernicharo et al., 2014). The NO<sup>+</sup>/NO ratio found in G+0.693 is also similar to the SO<sup>+</sup>/SO ratio (which is a factor of 1.7 higher) and a factor of  $\sim 50$  lower than the PO<sup>+</sup>/PO ratio.

## 4 DISCUSSION

### 4.1 Chemistry of PO<sup>+</sup>, NO<sup>+</sup>, and SO<sup>+</sup>

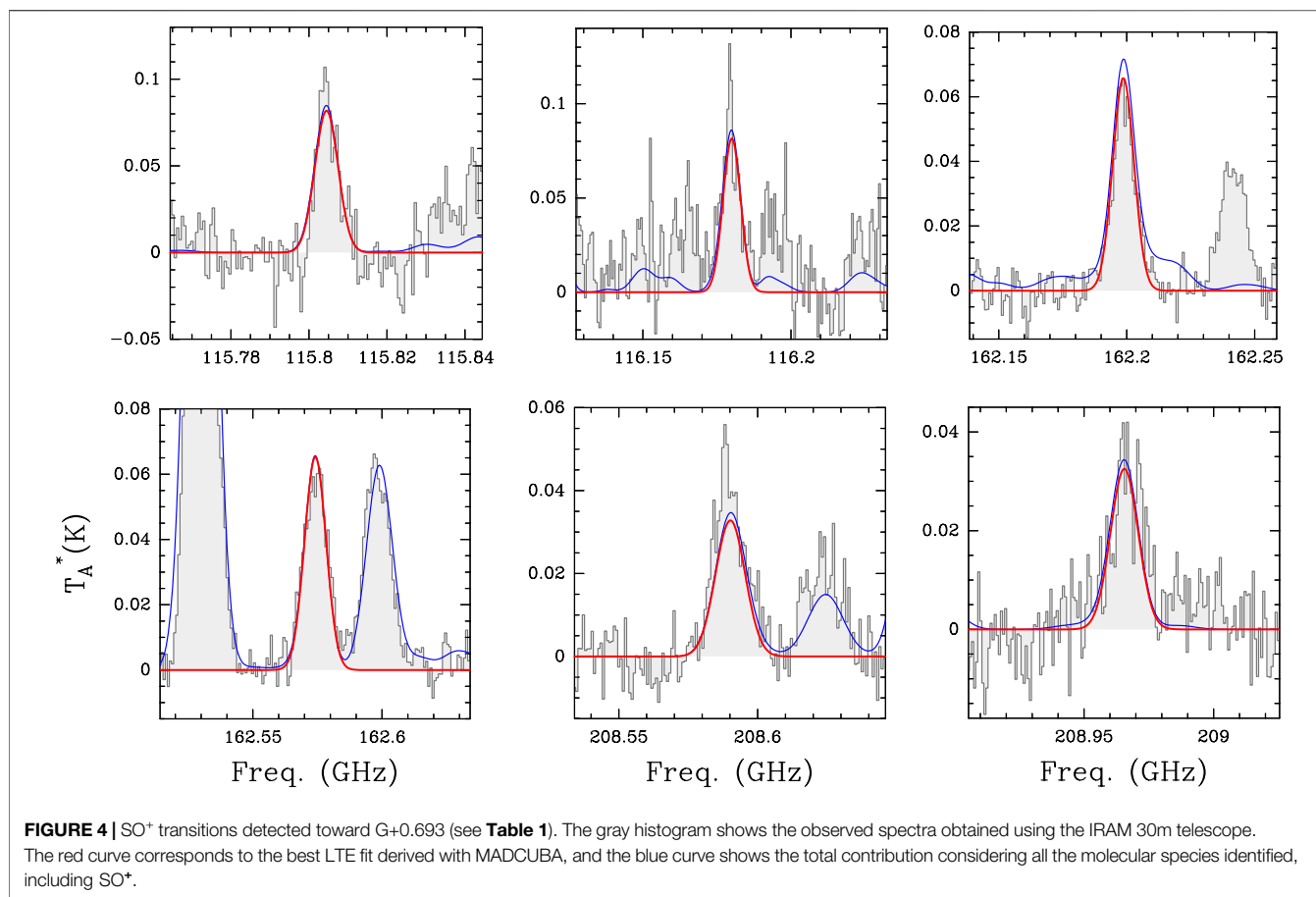
We discuss in this section the chemistry of PO<sup>+</sup>, so far poorly explored, comparing it with that of NO<sup>+</sup> and SO<sup>+</sup> proposed previously in the literature. Then, in **Section 4.2**, we present the results of a new detailed chemical modeling focused on the formation of PO<sup>+</sup>.

The upper panel of **Figure 9** shows the molecular column densities of NO<sup>+</sup>, SO<sup>+</sup>, and PO<sup>+</sup> and of their neutral counterparts derived in this work toward G+0.693. The two lowermost panels of **Figure 9** show the molecular abundances of the ion monoxides (middle lower panel) and the monoxides (lower panel),

normalized by the cosmic abundances of N, S, and P with respect to H (from Asplund et al., 2009). After the normalization by cosmic abundances, PO<sup>+</sup> is the most abundant ion; however, PO is the least abundant monoxide (two lowermost panels of **Figure 9**). These two facts together produce the observed enhancement of the  $N(\text{PO}^+)/N(\text{PO})$  ratio (middle upper panel of **Figure 9**), which is  $0.12 \pm 0.03$ , significantly higher than the  $N(\text{SO}^+)/N(\text{SO})$  ratio ( $0.0045 \pm 0.0003$ ) and the  $N(\text{NO}^+)/N(\text{NO})$  ratio ( $0.00245 \pm 0.00005$ ).

We discuss here the possible formations routes of these three ions, which are summarized in **Figure 10**. We have included the rates ( $k$ ) of the chemical reactions, obtained from KIDA (Kinetic Database for Astrochemistry, Wakelam et al., 2012) and the calculations of García de la Concepción et al. (2021). The values, indicated with numbers above each arrow, denote the  $\alpha$  parameter (in which the reaction constant is  $k = \alpha \times \zeta$ , with  $\zeta$  being the cosmic-ray ionization rate) for the cosmic-ray ionization reactions, and the values of  $k$  for the ion – molecule and electron recombination reactions are calculated at  $T = 100$  K, which is the average gas kinetic temperature of the CMZ (e.g. Huettemeister et al., 1993; Zeng et al., 2018).

Molecular ions are expected to be formed through gas-phase chemistry (e.g., Herbst and Leung 1986). For the case of SO<sup>+</sup>,

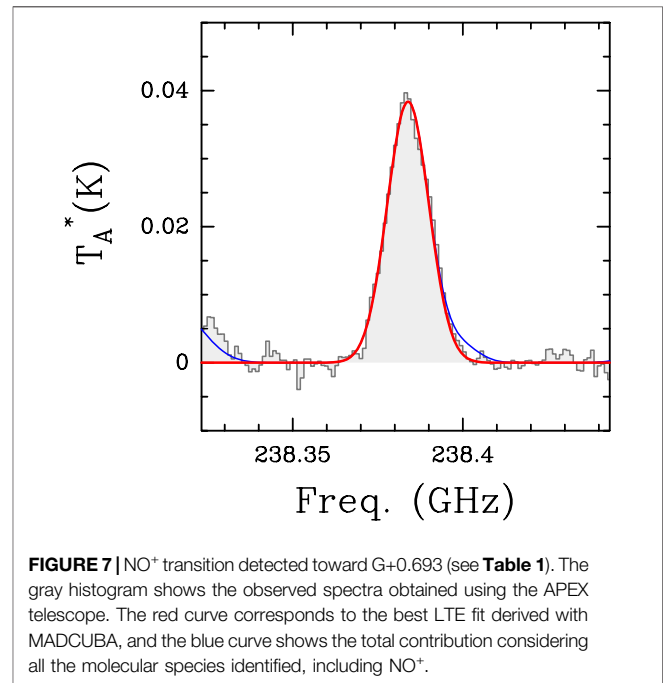
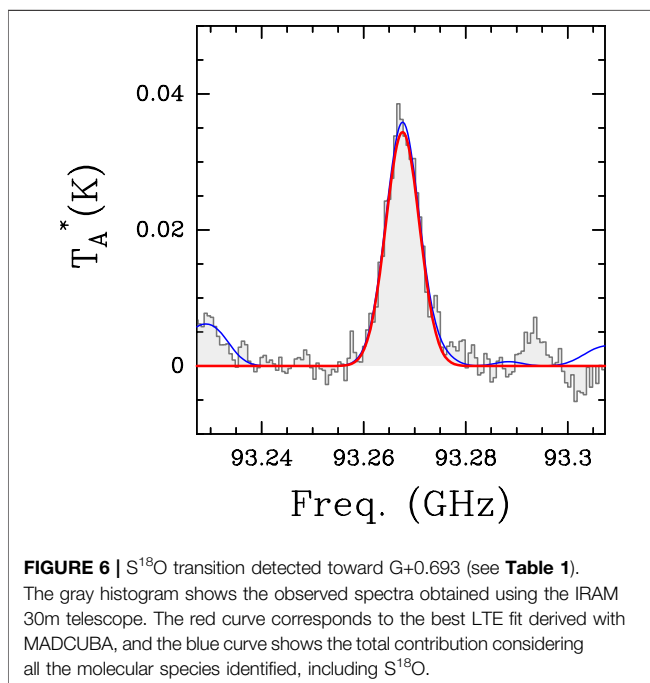
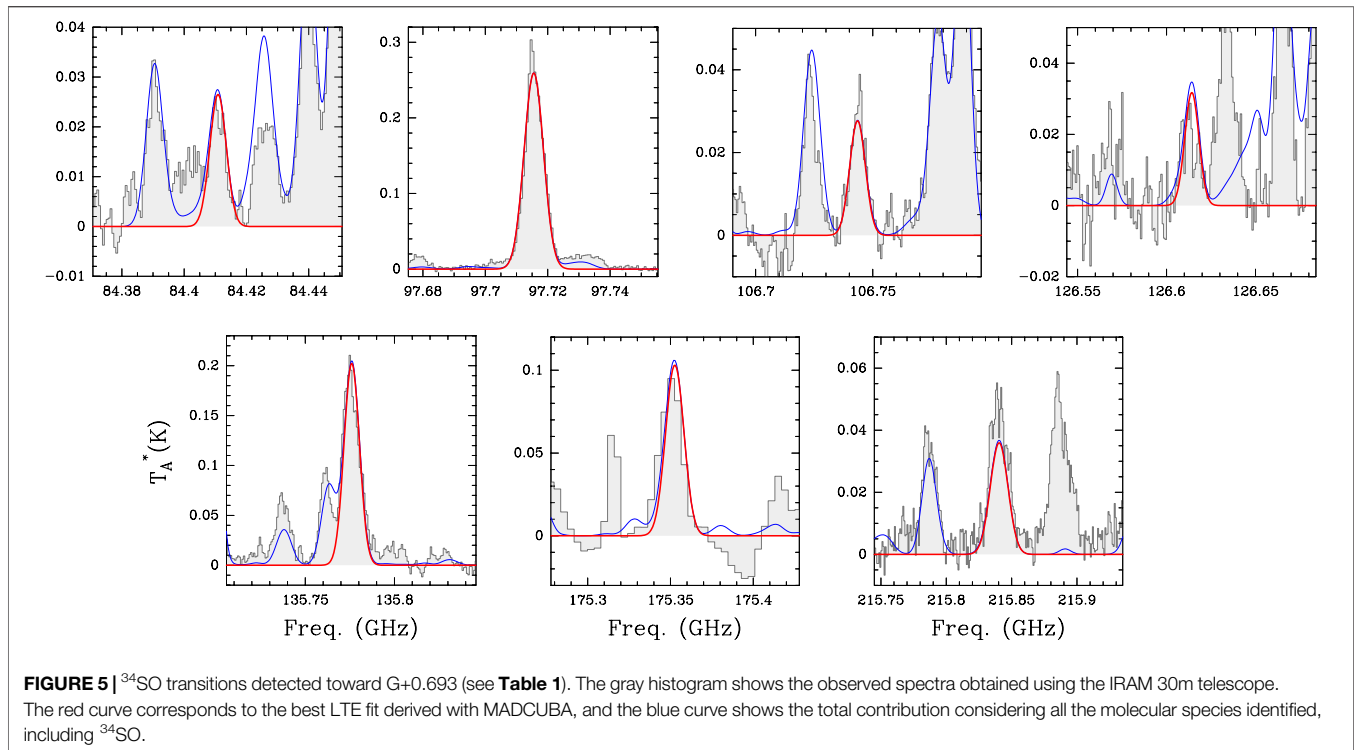


several works (Herbst and Leung 1989; Neufeld and Dalgarno 1989; Turner 1996) have shown that the dominant formation route of SO<sup>+</sup> is the ion–molecule reaction  $S^+ + OH \rightarrow SO^+ + H$ . Neufeld and Dalgarno (1989) argued that the SO<sup>+</sup> abundance can be strongly enhanced in shocked regions due to the release of S from dust mantles and its subsequent ionization by cosmic rays, followed by the previous reaction. This chemical pathway has been supported by the detection of SO<sup>+</sup> in the shocked molecular clump associated with the supernova remnant IC 443G (Turner 1992) and in the protostellar shock L1157 – B1 (Podio et al., 2014). The detection of SO<sup>+</sup> toward G+0.693, in which large-scale shocks are also present (e.g. Martín et al., 2008; Requena-Torres et al., 2008; Zeng et al., 2020), further confirms the primary shock origin of SO<sup>+</sup>. Moreover, the regions with enhanced cosmic-ray ionization rate, such as the CMZ in general (Goto et al., 2014) and G+0.693 in particular (Zeng et al., 2018) or the L1157 – B1 shock (Podio et al., 2014), favor the formation of S<sup>+</sup> through cosmic-ray ionization reactions (**Figure 10**), which also increase the formation efficiency of SO<sup>+</sup>.

Analogously, the same chemical route can be applied for N and P (left and right panels of **Figure 10**). In this scenario, NO<sup>+</sup> and PO<sup>+</sup> can be formed through  $N^+ + OH \rightarrow NO^+ + H$  and  $P^+ + OH \rightarrow PO^+ + H$ . The reaction rates of S<sup>+</sup>, N<sup>+</sup>, and P<sup>+</sup> with the OH radical, calculated by Woon and Herbst (2009), are similar regardless of the temperature (see, for e.g., the

values at 100 K in **Figure 10**). However, the observations indicate that the abundance of PO<sup>+</sup> after normalization by the cosmic abundance of P is higher than that of NO<sup>+</sup> and SO<sup>+</sup> (lower middle panel of **Figure 9**). This might be due to a higher cosmic-ray ionization of atomic P compared with that of N and S giving P<sup>+</sup>, N<sup>+</sup>, and S<sup>+</sup> (**Figure 9**). Indeed, the quantum calculations by Heays et al. (2017) indicate that the reaction rates of  $P \rightarrow P^+$  is higher than those of  $S \rightarrow S^+$  (by a factor of 1.8) and  $N \rightarrow N^+$  (by a factor of ~2000), as shown in **Figure 10**.

Another complementary chemical route for the formation of the monoxide ions (NO<sup>+</sup>, SO<sup>+</sup>, and PO<sup>+</sup>) is the cosmic-ray ionization of their neutral counterparts (NO, SO, and PO; **Figure 10**). The latter can be produced by gas-phase neutral reactions between atomic N, S, and P with the OH radical (Pineau des Forets et al., 1990; Turner 1996; Cernicharo et al., 2014; García de la Concepción et al., 2021). We note that they can also be formed with reactions with O<sub>2</sub> (KIDA and García de la Concepción et al., 2021), although the reaction rates are at least one order of magnitude lower. Previous observations have shown that the abundances of NO, SO, and PO are significantly enhanced in shocked regions (Bachiller and Pérez Gutiérrez 1997; Codella et al., 2018; Rivilla et al., 2018, 2020a), which make them abundant possible progenitors for their associated ions. For the case of S,



Turner (1992) found in the molecular clump IC 443C that SO<sup>+</sup> and SO do not coexist spatially, which seems to rule out this pathway, at least in this particular source. However, this might not be the case in other regions such as G+0.693, in which both species have been detected nor can be extrapolated to the cases of P and N.

As indicated in **Figure 10**, the rates of the reactions with OH to form the oxides are higher for P than for S and N by a factor of 3–4. However, the lower panel of **Figure 9** shows that the observed  $\chi(\text{PO})/\chi(\text{P})$  is lower than  $\chi(\text{NO})/\chi(\text{N})$  and  $\chi(\text{SO})/\chi(\text{S})$ . This might indicate that PO is more efficiently destroyed in the gas phase than SO and

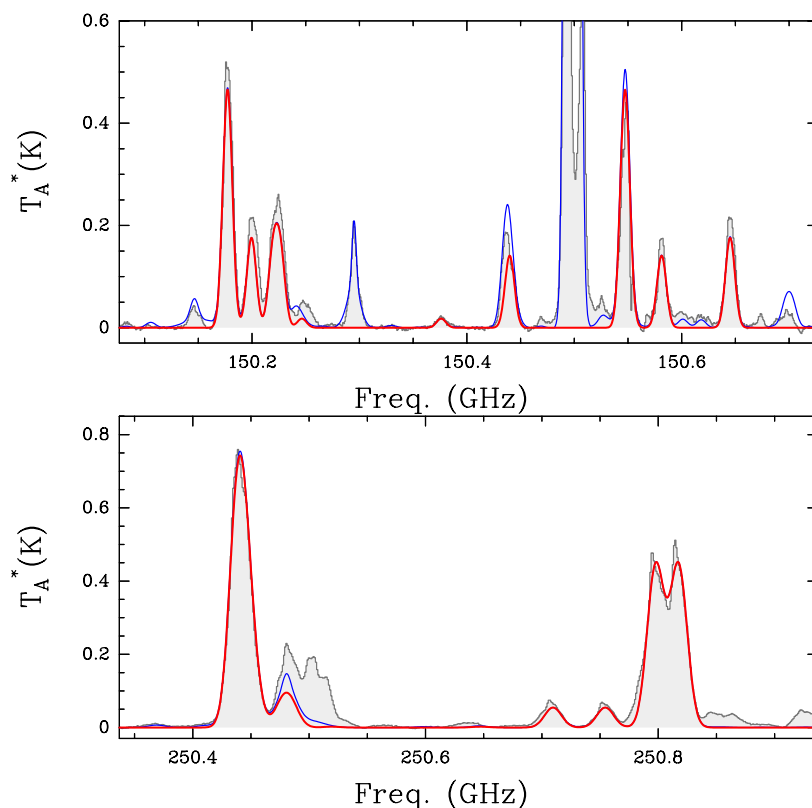


**FIGURE 8** | NO transitions detected toward G+0.693. The gray histograms show the observed spectra obtained using the IRAM 30m telescope (upper panel) and the APEX telescope (lower panel). The unblended transitions used to perform the fit with MADCUBA are listed in **Table 1**. The red curve corresponds to the best LTE fit derived with MADCUBA, and the blue curve shows the total contribution considering all the molecular species identified, including NO.

NO. In this sense, a possible destruction route would be the cosmic-ray ionization of PO to form  $\text{PO}^+$  (**Figure 10**). If this reaction were highly efficient, the abundance of PO would decrease, and the  $\text{PO}^+/\text{PO}$  ratio would be significantly enhanced, in agreement with observations. Unfortunately, this reaction is not included in the available chemical databases such as KIDA (Wakelam et al., 2012) or UMIST (McElroy et al., 2013), so its rate is not known. One can argue that the ionization rates of PO should be higher than those of SO and NO, as occurs for the atomic species (see values in **Figure 10**). P is the less electronegative atom; thus, the -I inductive effect produced by the O atom is more noticeable in PO than in SO or NO, as can be inferred from the dipole moments of the three oxides:  $\mu(\text{PO}) = 1.88 \text{ D} > \mu(\text{SO}) = 1.535 \text{ D} > \mu(\text{NO}) = 0.159 \text{ D}$  (**Appendix A**). As a consequence, the valence electrons on the P atom of PO are more weakly retained than in S of SO and much less than in N of NO. Furthermore, the highest occupied molecular orbital in PO is half-filled, being easier to lose an electron in comparison to the closed-shell orbital of SO. In **Section 4.2**, we have included the cosmic-ray ionization of PO in a chemical model to evaluate its role in the formation of  $\text{PO}^+$ .

Finally, the main destruction mechanism of the monoxide ions is the dissociative recombination reaction with electrons (blue arrows in

**Figure 10**), which produces back the atomic species.  $\text{NO}^+$  is more rapidly destroyed by electrons than  $\text{SO}^+$  and  $\text{PO}^+$ . This would further decrease the abundance of  $\text{NO}^+$ , which might explain why  $\chi(\text{NO}^+)/\chi(\text{N})$  and  $N(\text{NO}^+)/N(\text{NO})$  exhibit the lowest ratios (see **Figure 9**).

Regarding the still poorly constrained chemistry of P in the ISM, the relatively high gas-phase abundance of  $\text{PO}^+$  with respect to PO, in which  $N(\text{PO}^+)/N(\text{PO}) = 0.12 \pm 0.03$ , stresses the more predominant role that P-bearing ions such as  $\text{PO}^+$  and  $\text{P}^+$  can play in the chemical network of P than N and S chemistries. In the next section, we studied in more detail the formation of  $\text{PO}^+$  in G+0.693 using the chemical models of P chemistry presented in Jiménez-Serra et al. (2018).

## 4.2 Chemical Modeling of $\text{PO}^+$

To explain the abundances of  $\text{PO}^+$  measured in G+0.693, we have used the chemical code UCLCHEM<sup>4</sup> (Holdship et al., 2017) to simulate the P chemistry toward this source. It has been proposed that the chemistry of this source is characterized by low-velocity shocks (which explain the line widths of the molecular emission of  $20 \text{ km s}^{-1}$ ) and by an enhanced cosmic-ray ionization rate with respect to its standard value ( $\zeta_0 = 1.3 \times 10^{-13} \text{ s}^{-1}$ ).

<sup>4</sup><https://uclchem.github.io/>.

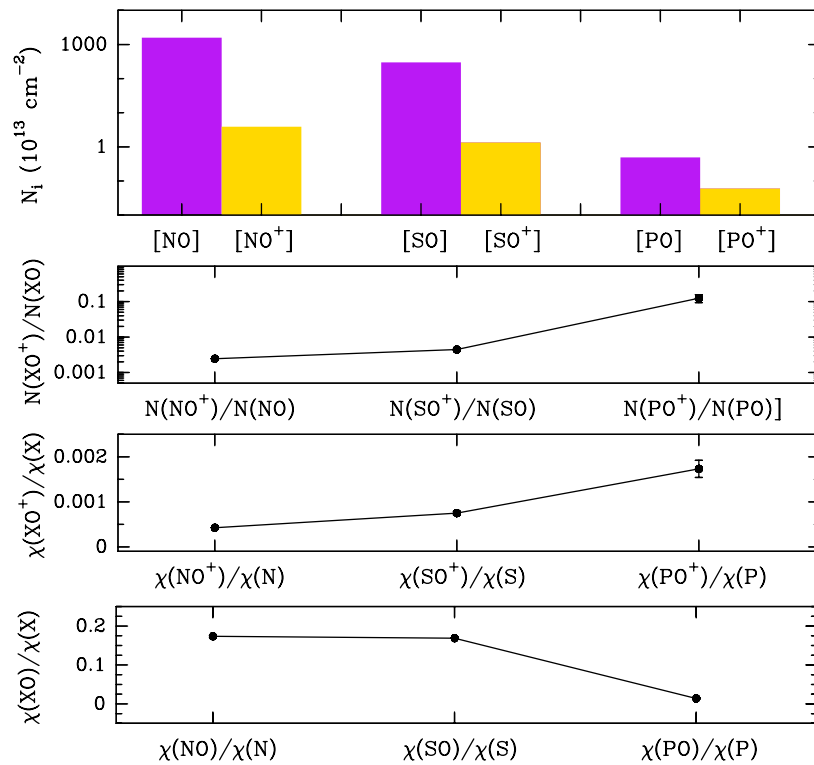


**FIGURE 9** | Upper panel: molecular column densities of the N, S, and P monoxides (purple) and ion monoxides (yellow) derived in G+0.693. Middle upper panel: molecular column density ratios of N, S, and P monoxides with respect to their associated ions in G+0.693. Middle lower panel: molecular abundances of NO<sup>+</sup>, SO<sup>+</sup>, and PO<sup>+</sup> normalized by the cosmic abundances of N, S, and P with respect to H. Cosmic abundances of N, S, and P are from Asplund et al., 2009. Lower panel: molecular abundances of NO, SO, and PO normalized by the cosmic abundances of N, S, and P with respect to H.

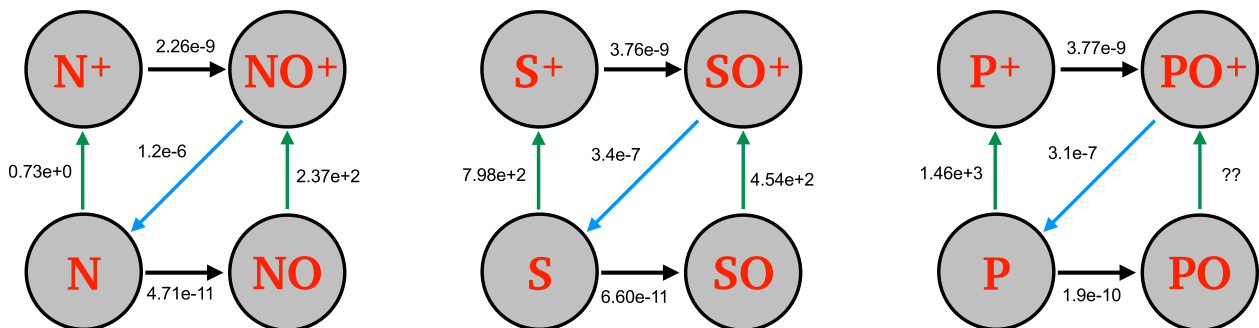
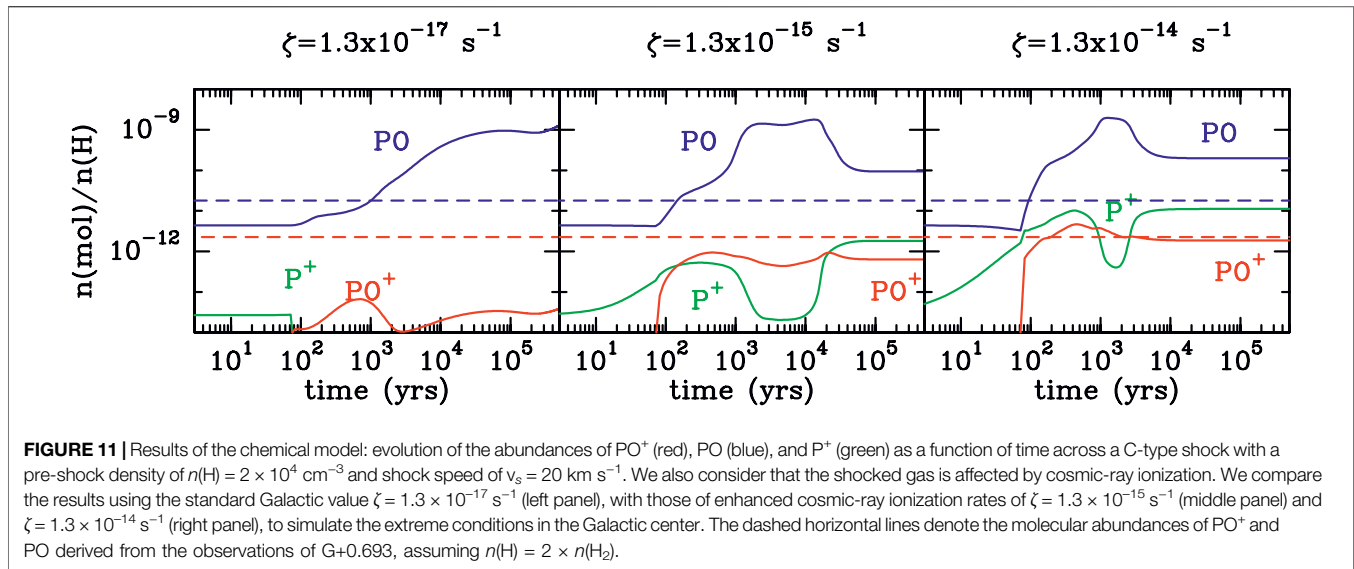


**FIGURE 10** | Chemical network of nitrogen, phosphorus, and sulfur monoxides and ion monoxides. The green arrows indicate cosmic-ray ionization reactions, the black arrows denote ion – molecule reactions with OH, and the blue arrows correspond to recombination with electron. The numbers indicate the values of  $\alpha$  (in which the reaction constant is  $k = \alpha \times \zeta$ ) for the cosmic-ray ionization reactions and the values of the  $k$  for the ion – molecule and electron recombination reactions (calculated at  $T = 100$  K).

UCLCHEM runs in three phases: Phase 0 considers the chemistry of a translucent cloud with  $n(\text{H}) = 10^3 \text{ cm}^{-3}$  and  $T_{\text{kin}} = 20$  K for  $10^6$  years. Phase 1 simulates the collapse of a molecular cloud from  $n(\text{H}) = 10^3 \text{ cm}^{-3}$  to  $n(\text{H}) = 2 \times 10^4 \text{ cm}^{-3}$  at a constant temperature of  $T_{\text{kin}} = 10$  K. At this stage, most of atomic P is locked into solid PH<sub>3</sub>. In Phase 2, we simulate the passage of a low-velocity C-type shock with  $v_s =$

$20 \text{ km s}^{-1}$  and an initial gas density of  $n(\text{H}) = 10^4 \text{ cm}^{-3}$  using the parametric approximation for the physical structure of the C-type shocks of Jiménez-Serra et al. (2008). The assumed shock velocity of  $v_s = 20 \text{ km}^{-1}$  is consistent with the observed line widths of the molecular line emission (Requena-Torres et al., 2006; Zeng et al., 2018) and with the gas densities measured toward G+0.693 (Zeng et al., 2020). The



maximum temperature reached within the shock is 900 K (see Table 4 in Jiménez-Serra et al., 2008). For the P chemistry network, we use the one built by Jiménez-Serra et al. (2018), which has recently been updated with the rates of the reactions  $\text{P} + \text{OH} \rightarrow \text{PO} + \text{H}$  and  $\text{P} + \text{H}_2\text{O} \rightarrow \text{PO} + \text{H}_2$  (García de la Concepción et al., 2021). The initial elemental abundances are as in Jiménez-Serra et al. (2018). In this work, we have implemented several updates:

1. The reaction rate of the ionization of P with a cosmic-ray photon (CR-photon), through the reaction  $\text{P} + \text{CR-photon} \rightarrow \text{P}^+ + \text{e}^-$ , was obtained from the quantum chemical calculations by Heays et al. (2017);
2. The reaction rate of  $\text{P}^+ + \text{OH} \rightarrow \text{PO}^+ + \text{H}$  was obtained from the calculations by Woon and Herbst (2009);
3. We have introduced for the first time the formation route of PO<sup>+</sup> proposed in this work:  $\text{PO} + \text{CR-photon} \rightarrow \text{PO}^+ + \text{e}^-$ . To our knowledge, there are neither laboratory experiments nor theoretical calculations carried out for this reaction. Therefore, we have assumed the rate of the analogous reaction with SO, from Heays et al. (2017). As discussed in Section 4.1, the ionization rate of PO might be higher than that of SO, so the value assumed here should be considered as a lower limit.

The chemistry of PO<sup>+</sup> is explored for three different values of the cosmic-ray ionization rate  $\zeta = 1.3 \times 10^{-17} \text{ s}^{-1}$ ,  $1.3 \times 10^{-15} \text{ s}^{-1}$ , and  $1.3 \times 10^{-14} \text{ s}^{-1}$ , i.e., 1, 100 and 1000 times the standard value. The results of Phase 2 of the models for the abundances of PO<sup>+</sup>, PO, and P<sup>+</sup> are shown in Figure 11 (solid curves), compared to the observed values of PO<sup>+</sup> and PO (dashed horizontal lines). It is clear that an enhanced cosmic-ray ionization rate of at least factors of 100–1000 is needed in order to obtain PO<sup>+</sup> abundances close to the observed value  $\sim 10^{-12}$ . In our models, most of the P contained on dust grains is in the form of PH<sub>3</sub>, which is initially released into the gas phase by the sputtering of the icy mantles once their saturation time-scale

is reached<sup>5</sup>. PH<sub>3</sub> is rapidly converted into P due to the endothermic destruction reactions  $\text{PH}_3 + \text{H} \rightarrow \text{PH}_2 + \text{H}_2$ ,  $\text{PH}_2 + \text{H} \rightarrow \text{PH} + \text{H}_2$ , and  $\text{PH} + \text{H} \rightarrow \text{P} + \text{H}_2$  and photo-dissociation by secondary ultraviolet photons (see Jiménez-Serra et al., 2018). Atomic P is then ionized efficiently with enhanced values of  $\zeta$ , as can be seen from the higher abundance of P<sup>+</sup> in the models with  $\zeta = 1.3 \times 10^{-15} \text{ s}^{-1}$  and  $1.3 \times 10^{-14} \text{ s}^{-1}$  (Figure 11), via the reaction  $\text{P} + \text{CR-photon} \rightarrow \text{P}^+ + \text{e}^-$ . This is consistent with the conclusion drawn in Section 4.1, of P being more easily ionized by cosmic rays than other elements such as N or S. In the model with  $\zeta = 1.3 \times 10^{-14} \text{ s}^{-1}$ , which reproduces better the observed abundance of PO<sup>+</sup>, the production of PO<sup>+</sup> is dominated by the reaction  $\text{P}^+ + \text{O}_2 \rightarrow \text{PO}^+ + \text{O}$  at early post-shock times (60–600 years), when O<sub>2</sub> is very abundant due to its release to the gas phase from the icy mantles after grain sputtering. Later, the production of PO<sup>+</sup> is dominated by the reaction  $\text{PO} + \text{CR-photon} \rightarrow \text{PO}^+$  until 2,500 years. After that time, PO<sup>+</sup> is mainly formed by  $\text{P}^+ + \text{OH} \rightarrow \text{PO}^+ + \text{H}$ , with a contribution of the  $\text{P}^+ + \text{O}_2$  pathway. We stress that we have assumed a reaction rate for the cosmic-ray ionization of PO, and that theoretical and experimental studies of this reaction would be helpful to evaluate its possible contribution to the formation of PO<sup>+</sup>.

## 5 SUMMARY AND CONCLUSION

We report the first detection of PO<sup>+</sup> in the interstellar medium, toward the molecular cloud G+0.693-0.027. We have detected the  $J = 1-0$  and  $J = 2-1$  transitions with the Yebes 40m and the IRAM 30m telescopes, respectively, which appear free of contamination from other species. The LTE analysis performed derives a column density of  $N = (6.0 \pm 0.7) \times 10^{11} \text{ cm}^{-2}$  and an abundance with respect

<sup>5</sup>The saturation time-scale is defined as the time at which 90% of the content of the icy mantles is sputtered off grains (see Jiménez-Serra et al., 2018).

to molecular hydrogen of  $4.5 \times 10^{-12}$ . The abundance of PO<sup>+</sup> normalized by the cosmic abundance of P is larger than that of NO<sup>+</sup> and SO<sup>+</sup>, normalized by N and S, by factors of 3.6 and 2.3, respectively. As well, the  $N(\text{PO}^+)/N(\text{PO})$  ratio is  $0.12 \pm 0.03$ , more than one order of magnitude higher than that of  $N(\text{SO}^+)/N(\text{SO})$  ( $0.0045 \pm 0.0003$ ) and  $N(\text{NO}^+)/N(\text{NO})$  ( $0.00264 \pm 0.00005$ ). These results indicate that P is more efficiently ionized in the ISM than N and S.

We have performed a detailed chemical model that includes the effects of a C-type shock and high cosmic-ray ionization rates ( $\zeta$ ), to reproduce the physical conditions of G+0.693. The results show that the abundance of PO<sup>+</sup> is enhanced in shocked regions with high values of  $\zeta$ . Most of the P contained on dust grains, which is in the form of PH<sub>3</sub>, is released into the gas phase by the sputtering of the icy mantles produced by the shock. PH<sub>3</sub> is rapidly converted into atomic P, which is then ionized efficiently by cosmic rays. Later, PO<sup>+</sup> is formed by the reactions of P<sup>+</sup> with O<sub>2</sub> at early post-shock times, and by cosmic-ray ionization of PO and by the reaction of P<sup>+</sup> with OH afterward. The values of the cosmic-ray ionization rates of  $\zeta = 10^{-15} - 10^{-14} \text{ s}^{-1}$  are needed to obtain PO<sup>+</sup> abundances close to the observed value of several  $10^{-12}$ . The relatively high gas-phase abundance of PO<sup>+</sup> with respect to PO,  $N(\text{PO}^+)/N(\text{PO}) = 0.12 \pm 0.03$  stresses the predominant role that P-bearing ions such as PO<sup>+</sup> and P<sup>+</sup> can play in the chemical network of P.

## DATA AVAILABILITY STATEMENT

The raw data supporting the conclusion of this article will be made available by the authors, without undue reservation.

## AUTHOR CONTRIBUTIONS

VR performed the data analysis and prepare the initial draft. VR, JM-P, IJ-S, BT, and GC designed and prepared the observations. JM-P, FR-V, and BT performed the observations. VR, JM-P, LC, IJ-S, AM, AL-G, AM-H, and SM reduced the raw data. JG performed the theoretical calculations of the dipole moments. IJ-S performed the chemical model. All coauthors revised the manuscript and contributed to the discussion.

## REFERENCES

- Adler, T. B., Knizia, G., and Werner, H.-J. (2007). A Simple and Efficient CCSD(T)-F12 Approximation. *J. Chem. Phys.* 127, 221106. doi:10.1063/1.2817618
- Agúndez, M., Cernicharo, J., Decin, L., Encrenaz, P., and Teyssier, D. (2014). Confirmation of Circumstellar Phosphine. *Astrophys J.* 790, L27. doi:10.1088/2041-8205/790/2/L27
- Agúndez, M., Cernicharo, J., and Guélin, M. (2007). Discovery of Phosphaethyne (HCP) in Space: Phosphorus Chemistry in Circumstellar Envelopes. *Astrophys J.* 662, L91–L94. doi:10.1086/519561
- Altwegg, K., Balsiger, H., Bar-Nun, A., Berthelier, J.-J., Bieler, A., Bochsler, P., et al. (2016). Prebiotic Chemicals-Amino Acid and Phosphorus-In the Coma of Comet 67P/Churyumov-Gerasimenko. *Sci. Adv.* 2, e1600285. doi:10.1126/sciadv.1600285

## FUNDING

VR, LC, and AL-G acknowledge the support from the Comunidad de Madrid through the Atracción de Talento Investigador Modalidad 1 (Doctores con experiencia) Grant (COOL: Cosmic Origins of Life; 2019-T1/TIC-15379). IJ-S and JM-P have received partial support from the Spanish State Research Agency (AEI) through project number PID 2019-105552RB-C41. JG acknowledges the Spanish State Research Agency (AEI) through project number MDM-2017-0737 Unidad de Excelencia “María de Maeztu”—Centro de Astrobiología and the Spanish State Research Agency (AEI) for partial financial support through Project No. PID 2019-105552RB-C41. Computational assistance was provided by the supercomputer facilities of LUSITANIA founded by the Cénits and Computaex Foundation.

## ACKNOWLEDGMENTS

We thank the two reviewers for their careful reading and helpful comments that have contributed to improve the original version of the manuscript. We are very grateful to the IRAM 30m, Yebes 40m, and APEX telescope staff for their precious help during the different observing runs. IRAM is supported by the National Institute for Universe Sciences and Astronomy/National Center for Scientific Research (France), Max Planck Society for the Advancement of Science (Germany), and the National Geographic Institute (IGN) (Spain). The 40m radio telescope at the Yebes Observatory is operated by the IGN, Ministerio de Transportes, Movilidad y Agenda Urbana. This publication is based on data acquired with the Atacama Pathfinder Experiment (APEX) under programmes ID O-0108.F-9308A-2021 and E-0108.C-0306A-2021. APEX is a collaboration between the Max-Planck-Institut für Radioastronomie, the European Southern Observatory, and the Onsala Space Observatory.

## SUPPLEMENTARY MATERIAL

The Supplementary Material for this article can be found online at: <https://www.frontiersin.org/articles/10.3389/fspas.2022.829288/full#supplementary-material>

- Amano, T., Amano, T., and Warner, H. E. (1991). The Microwave Spectrum of SO<sup>+</sup>. *J. Mol. Spectrosc.* 146, 519–523. doi:10.1016/0022-2852(91)90023-4
- Andersson, K., Malmqvist, P. A., Roos, B. O., Sadlej, A. J., and Wolinski, K. (1990). Second-order Perturbation Theory with a CASSCF Reference Function. *J. Phys. Chem.* 94, 5483–5488. doi:10.1021/j100377a012
- Asplund, M., Grevesse, N., Sauval, A. J., and Scott, P. (2009). The Chemical Composition of the Sun. *Annu. Rev. Astron. Astrophys.* 47, 481–522. doi:10.1146/annurev.astro.46.060407.145222
- Bachiller, R., and Pérez Gutiérrez, M. (1997). Shock Chemistry in the Young Bipolar Outflow L1157. *ApJL* 487, L93–L96. doi:10.1086/310877
- Bailleux, S., Bogey, M., Demuyneck, C., Liu, Y., and Walters, A. (2002). Millimeter-Wave Spectroscopy of PO in Excited Vibrational States up to V=7. *J. Mol. Spectrosc.* 216, 465–471. doi:10.1006/jmsp.2002.8665

- Ben Houria, A., Ben Lakhdar, Z., and Hochlaf, M. (2006). Spectroscopic and Spin-Orbit Calculations on the SO<sup>+</sup> Radical Cation. *J. Chem. Phys.* 124, 054313. doi:10.1063/1.2163872
- Bergner, J. B., Öberg, K. I., Walker, S., Guzmán, V. V., Rice, T. S., and Bergin, E. A. (2019). Detection of Phosphorus-Bearing Molecules toward a Solar-type Protostar. *Astrophys J.* 884, L36. doi:10.3847/2041-8213/ab48f9
- Bernal, J. J., Koelemay, L. A., and Ziurys, L. M. (2021). Detection of PO in Orion-KL: Phosphorus Chemistry in the Plateau Outflow. *Astrophys J.* 906, 55. doi:10.3847/1538-4357/abc87b
- Bowman, W. C., Herbst, E., and De Lucia, F. C. (1982). Millimeter and Submillimeter Spectrum of NO<sup>+</sup>. *J. Chem. Phys.* 77, 4261–4262. doi:10.1063/1.444307
- Bregman, J. D., Lester, D. F., and Rank, D. M. (1975). Observation of the Nu-Squared Band of PH<sub>3</sub> in the Atmosphere of Saturn. *Astrophys J.* 202, L55. doi:10.1086/181979
- Cernicharo, J., Bailleux, S., Alekseev, E., Fuente, A., Roueff, E., Gerin, M., et al. (2014). Tentative Detection of the Nitrosylium Ion in Space. *Astrophys J.* 795, 40. doi:10.1088/0004-637X/795/1/40
- Chantzou, J., Rivilla, V. M., Vasyunin, A., Redaelli, E., Bizzocchi, L., Fontani, F., et al. (2020). The First Steps of Interstellar Phosphorus Chemistry. *A&A* 633, A54. doi:10.1051/0004-6361/201936531
- Codella, C., Viti, S., Lefloch, B., Holdship, J., Bachiller, R., Bianchi, E., et al. (2018). Nitrogen Oxide in Protostellar Envelopes and Shocks: the ASAI Survey. *MNRAS* 474, 5694–5703. doi:10.1093/mnras/stx3196
- Colzi, L., Martín-Pintado, J., Rivilla, V. M., Jiménez-Serra, I., Zeng, S., Rodríguez-Almeida, L. F., et al. (2022). Deuterium Fractionation as a Multiphase Component Tracer in the Galactic Center. *ApJL* 926, L22. doi:10.3847/2041-8213/ac52ac
- Dyke, J. M., Morris, A., and Ridha, A. (1982). Study of the Ground State of PO<sup>+</sup> Using Photoelectron Spectroscopy. *J. Chem. Soc. Faraday Trans. 2* 78, 2077–2082. doi:10.1039/F29827802077
- Endres, C. P., Schlemmer, S., Schilke, P., Stutzki, J., and Müller, H. S. P. (2016). The Cologne Database for Molecular Spectroscopy, CDMS, in the Virtual Atomic and Molecular Data Centre, VAMDC. *J. Mol. Spectrosc.* 327, 95–104. doi:10.1016/j.jms.2016.03.005
- Fagerbakke, K., Heldal, M., and Norland, S. (1996). Content of Carbon, Nitrogen, Oxygen, Sulfur and Phosphorus in Native Aquatic and Cultured Bacteria. *Aquat. Microb. Ecol.* 10, 15–27. doi:10.3354/ame010015
- Feyereisen, M., Fitzgerald, G., and Komornicki, A. (1993). Use of Approximate Integrals in Ab Initio Theory. An Application in MP2 Energy Calculations. *Chem. Phys. Lett.* 208, 359–363. doi:10.1016/0009-2614(93)87156-W
- Fontani, F., Rivilla, V. M., Caselli, P., Vasyunin, A., and Palau, A. (2016). Phosphorus-bearing Molecules in Massive Dense Cores. *Astrophys J.* 822, L30. doi:10.3847/2041-8205/822/2/L30
- Fontani, F., Rivilla, V. M., van der Tak, F. F. S., Mininni, C., Beltrán, M. T., and Caselli, P. (2019). Origin of the PN Molecule in star-forming Regions: the Enlarged Sample. *MNRAS* 489, 4530–4542. doi:10.1093/mnras/stz2446
- García de la Concepción, J., Puzzarini, C., Barone, V., Jiménez-Serra, I., and Roncero, O. (2021). Formation of Phosphorus Monoxide (PO) in the Interstellar Medium: Insights from Quantum-Chemical and Kinetic Calculations. *arXiv e-prints*. arXiv:2108.08530.
- Goto, M., Geballe, T. R., Indriolo, N., Yusef-Zadeh, F., Usuda, T., Henning, T., et al. (2014). Infrared H<sub>2</sub><sup>+</sup> and CO Studies of the Galactic Core: Gcirs 3 and Gcirs 1W. *Astrophys J.* 786, 96. doi:10.1088/0004-637X/786/2/96
- Guelin, M., Cernicharo, J., Paubert, G., and Turner, B. E. (1990). Free CP in IRC +10216. *A&A* 230, L9–L11.
- Haasler, D., Rivilla, V. M., Martín, S., Holdship, J., Viti, S., Harada, N., et al. (2022). First Extragalactic Detection of a Phosphorus-Bearing Molecule with ALCHEMI: Phosphorus Nitride (PN). *AAP* 659, A158. doi:10.1051/0004-6361/202142032
- Halfen, D. T., Clouthier, D. J., and Ziurys, L. M. (2008). Detection of the CCP Radical (X 2 Π R) in IRC +10216: A New Interstellar Phosphorus-Containing Species. *Astrophys J.* 677, L101–L104. doi:10.1086/588024
- Heays, A. N., Bosman, A. D., and van Dishoeck, E. F. (2017). Photodissociation and Photoionisation of Atoms and Molecules of Astrophysical Interest. *A&A* 602, A105. doi:10.1051/0004-6361/201628742
- Herbst, E., and Leung, C. M. (1986). Effects of Large Rate Coefficients for Ion-Polar Neutral Reactions on Chemical Models of Dense Interstellar Clouds. *Astrophys J.* 310, 378. doi:10.1086/164691
- Herbst, E., and Leung, C. M. (1989). Gas-phase Production of Complex Hydrocarbons, Cyanopolynes, and Related Compounds in Dense Interstellar Clouds. *ApJS* 69, 271. doi:10.1086/191314
- Holdship, J., Viti, S., Jiménez-Serra, I., Makrýmalls, A., and Priestley, F. (2017). UCLCHEM: A Gas-Grain Chemical Code for Clouds, Cores, and C-Shocks. *AJ* 154, 38. doi:10.3847/1538-3881/aa773f
- Hüttelmeier, S., Wilson, T. L., Bania, T. M., and Martín-Pintado, J. (1993). Kinetic Temperatures in Galactic Center Molecular Clouds. *Astron. Astrophysics* 280, 255–267.
- Jiménez-Serra, I., Caselli, P., Martín-Pintado, J., and Hartquist, T. W. (2008). Parametrization of C-Shocks. Evolution of the Sputtering of Grains. *A&A* 482, 549–559. doi:10.1051/0004-6361:20078054
- Jiménez-Serra, I., Martín-Pintado, J., Rivilla, V. M., Rodríguez-Almeida, L., Alonso Alonso, E. R., Zeng, S., et al. (2020). Toward the RNA-World in the Interstellar Medium-Detection of Urea and Search of 2-Amino-Oxazole and Simple Sugars. *Astrobiology* 20, 1048–1066. doi:10.1089/ast.2019.2125
- Jiménez-Serra, I., Viti, S., Quénard, D., and Holdship, J. (2018). The Chemistry of Phosphorus-Bearing Molecules under Energetic Phenomena. *ApJ* 862, 128. doi:10.3847/1538-4357/aacdf2
- Jura, M., and York, D. G. (1978). Observations of Interstellar Chlorine and Phosphorus. *ApJ* 219, 861–869. doi:10.1086/155847
- Kanata, H., Yamamoto, S., and Saito, S. (1988). The Dipole Moment of the PO Radical Determined by Microwave Spectroscopy. *J. Mol. Spectrosc.* 131, 89–95. doi:10.1016/0022-2852(88)90109-9
- Kawaguchi, K., Saito, S., and Hirota, E. (1983). Far-infrared Laser Magnetic Resonance Detection and Microwave Spectroscopy of the PO Radical. *J. Chem. Phys.* 79, 629–634. doi:10.1063/1.445810
- Kendall, R. A., Dunning, T. H., and Harrison, R. J. (1992). Electron Affinities of the First-row Atoms Revisited. Systematic Basis Sets and Wave Functions. *J. Chem. Phys.* 96, 6796–6806. doi:10.1063/1.462569
- Knizia, G., Adler, T. B., and Werner, H.-J. (2009). Simplified CCSD(T)-F12 Methods: Theory and Benchmarks. *J. Chem. Phys.* 130, 054104. doi:10.1063/1.3054300
- Lee, T. J., and Taylor, P. R. (1989). A Diagnostic for Determining the Quality of Single-Reference Electron Correlation Methods. *Int. J. Quan. Chem.* 36, 199–207. doi:10.1002/qua.560360824
- Lefloch, B., Vastel, C., Viti, S., Jiménez-Serra, I., Codella, C., Podio, L., et al. (2016). Phosphorus-bearing Molecules in Solar-type star-forming Regions: First PO Detection. *Mon. Not. R. Astron. Soc.* 462, 3937–3944. doi:10.1093/mnras/stw1918
- Lovas, F. J., Suenram, R. D., Ogata, T., and Yamamoto, S. (1992). Microwave Spectra and Electric Dipole Moments for Low-J Levels of Interstellar Radicals: SO, C<sub>2</sub>S, C<sub>3</sub>S, C-HC<sub>3</sub>, CH<sub>2</sub>CC, and C-C<sub>3</sub>H<sub>2</sub>. *Astrophys J.* 399, 325. doi:10.1086/171928
- Mancini, L., Rosi, M., Balucani, N., Skouteris, D., Codella, C., and Ceccarelli, C. (2020). “Probing the Chemistry of P-Bearing Molecules in Interstellar Environments and Other Extraterrestrial Environments,” in *European Planetary Science Congress. EPSC2020–643*.
- Martin, S., Martín-Pintado, J., Blanco-Sánchez, C., Rivilla, V. M., Rodríguez-Franco, A., and Rico-Villas, F. (2019). Spectral Line Identification and Modelling (SLIM) in the MADrid Data CUBe Analysis (MADCUBA) Package. *A&A* 631, A159. doi:10.1051/0004-6361/201936144
- Martin, S., Requena-Torres, M. A., Martín-Pintado, J., and Mauersberger, R. (2008). Tracing Shocks and Photodissociation in the Galactic center Region. *Astrophysical J.* 678, 245–254. doi:10.1086/533409
- McElroy, D., Walsh, C., Markwick, A. J., Cordiner, M. A., Smith, K., and Millar, T. J. (2013). The UMIST Database for Astrochemistry 2012. *A&A* 550, A36. doi:10.1051/0004-6361/201220465
- Mininni, C., Fontani, F., Rivilla, V. M., Beltrán, M. T., Caselli, P., and Vasyunin, A. (2018). On the Origin of Phosphorus Nitride in star-forming Regions. *MNRAS* 476, L39–L44. doi:10.1093/mnras/sly026
- Moussaoui, Y., Ouamerli, O., and De Maré, G. R. (2003). Properties of the Phosphorus Oxide Radical, PO, its Cation and Anion in Their Ground Electronic States: Comparison of Theoretical and Experimental Data. *Int. Rev. Phys. Chem.* 22, 641–675. doi:10.1080/01442350310001617011

- Müller, H. S. P., Kobayashi, K., Takahashi, K., Tomaru, K., and Matsushima, F. (2015). Terahertz Spectroscopy of N18O and Isotopic Invariant Fit of Several Nitric Oxide Isotopologs. *J. Mol. Spectrosc.* 310, 92–98. doi:10.1016/j.jms.2014.12.002
- Neufeld, D. A., and Dalgarno, A. (1989). Fast Molecular Shocks. I - Reformation of Molecules behind a Dissociative Shock. *Astrophys J.* 340, 869. doi:10.1086/167441
- Neumann, R. M. (1970). High-Precision Radiofrequency Spectrum of  $\{^{14}\text{N}\}^{16}\text{O}$ . *Astrophys J.* 161, 779. doi:10.1086/150578
- Padovani, M., Galli, D., and Glassgold, A. E. (2009). Cosmic-ray Ionization of Molecular Clouds. *A&A* 501, 619–631. doi:10.1051/0004-6361/200911794
- Pasek, M. A., and Lauretta, D. S. (2005). Aqueous Corrosion of Phosphide Minerals from Iron Meteorites: A Highly Reactive Source of Prebiotic Phosphorus on the Surface of the Early Earth. *Astrobiology* 5, 515–535. doi:10.1089/ast.2005.5.515
- Peterson, K. A., and Woods, R. C. (1990). Configuration Interaction Potential Energy and Dipole Moment Functions for Thirteen 22 Electron Diatomics. *J. Chem. Phys.* 92, 6061–6068. doi:10.1063/1.458378
- Peterson, K. A., Woon, D. E., and Dunning, T. H. (1994). Benchmark Calculations with Correlated Molecular Wave Functions. IV. The Classical Barrier Height of the  $\text{H}+\text{H}_2\rightarrow\text{H}_2+\text{H}$  Reaction. *J. Chem. Phys.* 100, 7410–7415. doi:10.1063/1.466884
- Petrnichl, R. H., Peterson, K. A., and Woods, R. C. (1991). The Microwave Spectrum of PO<sup>+</sup>: Comparison to SiF<sup>+</sup>. *J. Chem. Phys.* 94, 3504–3510. doi:10.1063/1.459771
- Pickett, H. M., Poynter, R. L., Cohen, E. A., Delitsky, M. L., Pearson, J. C., and Müller, H. S. P. (1998). Submillimeter, Millimeter, and Microwave Spectral Line Catalog. *J. Quantitative Spectrosc. Radiative Transfer* 60, 883–890. doi:10.1016/S0022-4073(98)00091-0
- Pineau des Forets, G., Roueff, E., and Flower, D. R. (1990). The Formation of Nitrogen-Bearing Species in Dark Interstellar Clouds. *MNRAS* 244, 668–674.
- Podio, L., Lefloch, B., Ceccarelli, C., Codella, C., and Bachiller, R. (2014). Molecular Ions in the Protostellar Shock L1157-B1. *A&A* 565, A64. doi:10.1051/0004-6361/201322928
- Polák, R., and Fišer, J. (2004). A Comparative icMRCI Study of Some NO<sup>+</sup>, NO and NO<sup>-</sup> Electronic Ground State Properties. *Chem. Phys.* 303, 73–83. doi:10.1016/j.chemphys.2004.04.027
- Powell, F. X., and Lide, D. R. (1964). Microwave Spectrum of the So Radical. *J. Chem. Phys.* 41, 1413–1419. doi:10.1063/1.1726082
- Requena-Torres, M. A., Martín-Pintado, J., Martín, S., and Morris, M. R. (2008). The Largest Oxygen Bearing Organic Molecule Repository. *Astrophysical J.* 672, 352–360. doi:10.1086/523627
- Requena-Torres, M. A., Martín-Pintado, J., Rodríguez-Franco, A., Martín, S., Rodríguez-Fernández, N. J., and de Vicente, P. (2006). Organic Molecules in the Galactic center. *A&A* 455, 971–985. doi:10.1051/0004-6361:20065190
- Ridgway, S. T., Wallace, L., and Smith, G. R. (1976). The 800-1200 Inverse Centimeter Absorption Spectrum of Jupiter. *Astrophys J.* 207, 1002–1006. doi:10.1086/154570
- Rienstra-Kiracofe, J. C., Allen, W. D., and Schaefer, H. F. (2000). The C<sub>2</sub>H<sub>5</sub> + O<sub>2</sub> Reaction Mechanism: High-Level Ab Initio Characterizations. *J. Phys. Chem. A.* 104, 9823–9840. doi:10.1021/jp001041k
- Rivilla, V. M., Beltrán, M. T., Vasyunin, A., Caselli, P., Viti, S., Fontani, F., et al. (2019). First ALMA Maps of HCO, an Important Precursor of Complex Organic Molecules, towards IRAS 16293-2422. *MNRAS* 483, 806–823. doi:10.1093/mnras/sty3078
- Rivilla, V. M., Drozdovskaya, M. N., Altwegg, K., Caselli, P., Beltrán, M. T., Fontani, F., et al. (2020a). ALMA and ROSINA Detections of Phosphorus-Bearing Molecules: the Interstellar Thread between star-forming Regions and Comets. *MNRAS* 492, 1180–1198. doi:10.1093/mnras/stz3336
- Rivilla, V. M., Fontani, F., Beltrán, M. T., Vasyunin, A., Caselli, P., Martín-Pintado, J., et al. (2016). The First Detections of the Key Prebiotic Molecule PO in Star-forming Regions. *Astrophys J.* 826, 161. doi:10.3847/0004-637x/826/2/161
- Rivilla, V. M., Jiménez-Serra, I., García de la Concepción, J., Martín-Pintado, J., Colzi, L., Rodríguez-Almeida, L. F., et al. (2021b). Detection of the Cyanomethyl Radical (HNCN): a New Interstellar Species with the NCN Backbone. *MNRAS* 506, L79–L84. doi:10.1093/mnras/slab074
- Rivilla, V. M., Jiménez-Serra, I., Martín-Pintado, J., Briones, C., Rodríguez-Almeida, L. F., Rico-Villas, F., et al. (2021a). Discovery in Space of Ethanolamine, the Simplest Phospholipid Head Group. *Proc. Natl. Acad. Sci. U.S.A.* 118. doi:10.1073/pnas.2101314118
- Rivilla, V. M., Jiménez-Serra, I., Zeng, S., Martín, S., Martín-Pintado, J., Armijos-Abendaño, J., et al. (2018). Phosphorus-bearing Molecules in the Galactic Center. *MNRAS* 475, L30–L34. doi:10.1093/mnras/slx208
- Rivilla, V. M., Martín-Pintado, J., Jiménez-Serra, I., Martín, S., Rodríguez-Almeida, L. F., Requena-Torres, M. A., et al. (2020b). Prebiotic Precursors of the Primordial RNA World in Space: Detection of NH<sub>2</sub>OH. *Astrophys J.* 899, L28. doi:10.3847/2041-8213/abac55
- Roca-Sanjuán, D., Aquilante, F., and Lindh, R. (2012). Multiconfiguration Second-Order Perturbation Theory Approach to strong Electron Correlation in Chemistry and Photochemistry. *Wires Comput. Mol. Sci.* 2, 585–603. doi:10.1002/wcms.97
- Rodríguez-Almeida, L. F., Jiménez-Serra, I., Rivilla, V. M., Martín-Pintado, J., Zeng, S., Tercero, B., et al. (2021a). Thiols in the Interstellar Medium: First Detection of HC(O)SH and Confirmation of C<sub>2</sub>H<sub>5</sub>SH. *ApJL* 912, L11. doi:10.3847/2041-8213/abf7cb
- Rodríguez-Almeida, L. F., Rivilla, V. M., Jiménez-Serra, I., Melosso, M., Colzi, L., Zeng, S., et al. (2021b). First Detection of C<sub>2</sub>H<sub>5</sub>NCO in the ISM and Search of Other Isocyanates towards the G+0.693-0.027 Molecular Cloud. *A&A* 654, L1. doi:10.1051/0004-6361/202141989
- Schwartz, A. W. (2006). Phosphorus in Prebiotic Chemistry. *Phil. Trans. R. Soc. B* 361, 1743–1749. doi:10.1098/rstb.2006.1901
- Tenenbaum, E. D., Woolf, N. J., and Ziurys, L. M. (2007). Identification of Phosphorus Monoxide ( X 2 Π R ) in VY Canis Majoris: Detection of the First P-O Bond in Space. *Astrophys J.* 666, L29–L32. doi:10.1086/521361
- Tercero, F., López-Pérez, J. A., Gallego, J. D., Beltrán, F., García, O., Patino-Esteban, M., et al. (2021). Yebe 40 M Radio Telescope and the Broad Band Nanocosmos Receivers at 7 Mm and 3 Mm for Line Surveys. *A&A* 645, A37. doi:10.1051/0004-6361/202038701
- Thorne, L. R., Anicich, V. G., Prasad, S. S., and Huntress, W. T. J. (1984). The Chemistry of Phosphorus in Dense Interstellar Clouds. *Astrophys J.* 280, 139–143. doi:10.1086/161977
- Tiemann, E. (1974). Microwave Spectra of Molecules of Astrophysical Interest VIII. Sulfur Monoxide. *J. Phys. Chem. Reference Data* 3, 259–268. doi:10.1063/1.3253141
- Turner, B. E., and Bally, J. (1987). Detection of Interstellar PN - the First Identified Phosphorus Compound in the Interstellar Medium. *Astrophys J.* 321, L75–L79. doi:10.1086/185009
- Turner, B. E. (1992). Detection of Interstellar SO(+) - A Diagnostic of Dissociative Shock Chemistry. *Astrophys J.* 396, L107. doi:10.1086/186528
- Turner, B. E. (1996). The Physics and Chemistry of Small Translucent Molecular Clouds. VII. SO + and H 2S. *Astrophys J.* 468, 694. doi:10.1086/177727
- Wakelam, V., Herbst, E., Loison, J.-C., Smith, I. W. M., Chandrasekaran, V., Pavone, B., et al. (2012). A Kinetic Database for Astrochemistry (KIDA). *ApJS* 199, 21. doi:10.1088/0067-0049/199/1/21
- Wilson, A. K., van Mourik, T., and Dunning, T. H. (1996). Gaussian Basis Sets for Use in Correlated Molecular Calculations. VI. Sextuple Zeta Correlation Consistent Basis Sets for boron through Neon. *J. Mol. Struct. THEOCHEM* 388, 339–349. doi:10.1016/S0166-1280(96)80048-0
- Wilson, T. L., and Rood, R. T. (1994). Abundances in the Interstellar Medium. *Annu. Rev. Astron. Astrophys.* 32, 191–226. doi:10.1146/annurev.aa.32.090194.001203
- Woon, D. E., and Dunning, T. H. (1993). Gaussian Basis Sets for Use in Correlated Molecular Calculations. III. The Atoms Aluminum through Argon. *J. Chem. Phys.* 98, 1358–1371. doi:10.1063/1.464303
- Woon, D. E., and Herbst, E. (2009). Quantum Chemical Predictions of the Properties of Known and Postulated Neutral Interstellar Molecules. *ApJS* 185, 273–288. doi:10.1088/0067-0049/185/2/273
- Xing, W., Shi, D., Sun, J., and Zhu, Z. (2012). Investigation of Spectroscopic Properties and Spin-Orbit Splitting in the X<sup>2</sup>Π and A<sup>2</sup>Π Electronic States of the SO<sup>+</sup> Cation. *Int. J. Mol. Sci.* 13, 8189–8209. doi:10.3390/ijms13078189
- Zeng, S., Jiménez-Serra, I., Rivilla, V. M., Martín, S., Martín-Pintado, J., Requena-Torres, M. A., et al. (2018). Complex Organic Molecules in the Galactic Centre: the N-Bearing Family. *Monthly Notices R. Astronomical Soc.* 478, 2962–2975. doi:10.1093/mnras/sty1174
- Zeng, S., Jiménez-Serra, I., Rivilla, V. M., Martín-Pintado, J., Rodríguez-Almeida, L. F., Tercero, B., et al. (2021). Probing the Chemical Complexity of Amines in the ISM:

- Detection of Vinylamine (C<sub>2</sub>H<sub>3</sub>NH<sub>2</sub>) and Tentative Detection of Ethylamine (C<sub>2</sub>H<sub>5</sub>NH<sub>2</sub>). *ApJL* 920, L27. doi:10.3847/2041-8213/ac2c7e
- Zeng, S., Zhang, Q., Jiménez-Serra, I., Tercero, B., Lu, X., Martín-Pintado, J., et al. (2020). Cloud-cloud Collision as Drivers of the Chemical Complexity in Galactic Centre Molecular Clouds. *MNRAS* 497, 4896–4909. doi:10.1093/mnras/staa2187
- Zhang, M., and Shi, D. (2021). Transition Properties of X1Σ<sup>+</sup>, A1Σ<sup>-</sup>, B1Δ, C1Π, A3Σ<sup>+</sup>, B3Δ, C3Π, and D3Σ<sup>-</sup> States of PO<sup>+</sup>. *J. Quantitative Spectrosc. Radiative Transfer* 264, 107553. doi:10.1016/j.jqsrt.2021.107553
- Ziurys, L. M. (1987). Detection of Interstellar PN - the First Phosphorus-Bearing Species Observed in Molecular Clouds. *Astrophys J.* 321, L81. doi:10.1086/185010

**Conflict of Interest:** The authors declare that the research was conducted in the absence of any commercial or financial relationships that could be construed as a potential conflict of interest.

**Publisher's Note:** All claims expressed in this article are solely those of the authors and do not necessarily represent those of their affiliated organizations, or those of the publisher, the editors, and the reviewers. Any product that may be evaluated in this article, or claim that may be made by its manufacturer, is not guaranteed or endorsed by the publisher.

Copyright © 2022 Rivilla, García De La Concepción, Jiménez-Serra, Martín-Pintado, Colzi, Tercero, Megías, López-Gallifa, Martínez-Henares, Massalkhi, Martín, Zeng, De Vicente, Rico-Villas, Requena-Torres and Cosentino. This is an open-access article distributed under the terms of the Creative Commons Attribution License (CC BY). The use, distribution or reproduction in other forums is permitted, provided the original author(s) and the copyright owner(s) are credited and that the original publication in this journal is cited, in accordance with accepted academic practice. No use, distribution or reproduction is permitted which does not comply with these terms.